

P. K. Panigrahi · A. Schröder · J. Kompenhans

PIV investigation of flow behind surface mounted permeable ribs

Received: 24 March 2005 / Revised: 10 June 2005 / Accepted: 29 September 2005 / Published online: 23 November 2005
© Springer-Verlag 2005

Abstract The flow behind surface mounted permeable rib geometries, i.e. solid, slit, split-slit and inclined split-slit ribs have been studied using flow visualization and PIV (2-C and 3-C) technique in streamwise and cross-stream measurement planes. The objective behind this study is to understand the flow structures responsible for heat transfer/mixing enhancement with simultaneous pressure penalty reduction by permeable rib geometries. The Reynolds number based on the rib height has been set equal to 5,538 and the open area ratio of permeable ribs is equal to 20%. The permeable rib geometries have shorter reattachment length in comparison to the solid rib. The maximum 41% reduction in reattachment length is observed for the inclined split-slit rib. The splitter mounted inside the slit leads to two corner vortices behind it. The corner vortices drag the flow from the primary recirculation bubble region towards the rib resulting in drop of the reattachment length. Two horseshoe vortices are present in the flow through the slit at both sides of the splitter due to the upstream flow separation. The slit inclination moves these horseshoe vortices closer to the bottom wall. A film like flow through the slit is present near the downstream corner of the inclined split-slit rib. The spanwise velocity gradient due to the splitter leads to vorticity and turbulence enhancement by vortex stretching. The inclination of the slit and the use of a splitter inside the slit are two important design parameters responsible in generation of near-wall longitudinal vortices. The flow field behind permeable ribs is dominated by vortical structures with definable critical flow patterns, i.e. node, saddle and

foci. These predominant swirling flow motions contribute to the mixing enhancement behind permeable rib geometries.

Nomenclature

X, Y	Spatial coordinates
Z	
u, v	Mean velocity components
w	
h	Rib height
V	Velocity vector magnitude
Q	Velocity gradient tensor invariant
S	Symmetric part of velocity gradient tensor
X_R	Reattachment length
U^+	Normalized velocity in wall coordinate
Y^+	Normalized Y in wall coordinate
U_τ	Wall shear velocity
U_o	Free stream velocity
δ	Boundary layer thickness
δ^*	Displacement thickness
θ	Momentum thickness
Ψ	Stream function
λ	Eigen value
ω	Vorticity
Ω	Antisymmetric part of velocity gradient tensor
rms	Root mean square
$\langle \rangle$	Time averaged value of quantity

On leave from Mechanical Engineering Department, IIT Kanpur, U.P. 208016, India

P. K. Panigrahi (✉) · A. Schröder · J. Kompenhans
Institute of Aerodynamics and Flow Technology,
German Aerospace Center, Bunsenstrasse 10,
Goettingen, 37073, Germany
E-mail: panig@iitk.ac.in

1 Introduction

The use of periodic roughness elements, i.e. ribs, delta wings etc. to enhance the heat transfer and mixing is a well-established approach practiced in heat exchangers, nuclear reactor fuel elements and cooling passages of the gas turbine blades. The flow past the roughness elements leads to separation due to sudden expansion and subsequent reattachment downstream with a recirculating region located both upstream and downstream. The

reattaching flow is highly 3D and unsteady, which redevelops to a turbulent boundary layer state in the downstream region. Previous investigations to this complex flow have primarily used single point measurement techniques, i.e. hot wire anemometry, laser Doppler velocimetry, flow visualization and 2-C particle image velocimetry. The advent of multi-dimensional particle image velocimetry (3-C stereo PIV) is well suited to study the instantaneous flow structures and dynamics of these flows. Few experimental investigations related to the reattaching flow and their control behind the surface mounted ribs showing the spatiotemporal structures have been carried out and are briefly described below.

Takase (1996) evaluated the thermal hydraulic performance of rib-roughened fuel rod annulus in a helium-cooled graphite high temperature reactor. The development of high heat flux fuel rods leads to increase power density in the reactor core and therefore demands better heat transfer from safety point of view. The comparison of a spacer rib configuration with that of the square rib showed superior overall heat transfer performance of the square ribbed configuration. Gentry and Jacobi (1997) studied the delta-wing vortex generators relevant to heat exchanger applications using laser flow visualization and Naphthalene sublimation technique. They demonstrated about 50% average heat transfer enhancement by delta-wing vortex generators mounted on the flat plate. The generated streamwise vortices due to the delta wing advect the free stream fluid into the boundary layer and effectively thin the boundary layer. Islam et al. (2002) investigated the turbulent water flow structure over micro-repeated ribs in a narrow 2-D rectangular channel by particle image velocimetry (2-C PIV). They observed no significant effect of the pitch and Reynolds number on the reattachment length beyond a critical value of Reynolds number. Iacovides et al. (2003) investigated the turbulent flow and heat transfer with 45° staggered ribs in a duct configuration relevant to the cooling of gas turbine blades. They showed the role played by rib inclination in inducing secondary motions, which redistribute the streamwise momentum across the ducts. The high turbulence level generated by the rib-induced separation is also influenced by this secondary motion. The influence of turbulence on the flow and thermal development for the inclined rib is reduced in comparison to the normal rib due to the influence of these secondary structures. Gao and Sunden (2004) simulated the heat transfer inside compact heat exchangers, i.e. car radiators using different circular cross-section rib configurations, i.e. staggered parallel ribs, in-line parallel ribs, crossed ribs and v-shaped ribs pointing upstream and downstream. The 2-C PIV at different measurement planes was used. The results showed strong effects of rib inclination on the flow behaviour due to the secondary flow development. The secondary flow generated along the inclined rib acts as an additional heat transfer mechanism in elevating the heat transfer to a higher level. Calluaud and David (2004) investigated the 3D

features of the flow around a surface-mounted block using stereoscopic particle image velocimetry. The 3D calibration was carried out based on a real linear camera model, which does not require the introduction of parameters and knowledge of the geometric configuration of the stereoscopic system in order to determine the calibration matrices. They showed the accuracy of their calibration approach and stressed the need for 3-C PIV measurements in 3-D flows.

Different passive control techniques have been proposed for control of the reattaching flow. Heenan and Morrison (1998) presented the passive control of backward facing step flow using a permeable reattachment surface of open area ratio equal to 20%. The permeable reattachment surface dampens the impinging vortical structures and a steady upstream flow travels towards the backstep. This mode of control looks promising for reduction of deleterious effects due to the low frequency unsteadiness or flapping on aircraft wing components. Permeable rib geometries have been proposed by various investigators and shown to be more effective than the solid rib. Hwang (1998) investigated the effect of interrupted slits in a rib on heat transfer of a rectangular channel using laser holographic interferometry and observed superior heat transfer performance of the slit-ribbed channel. Liou et al. (2002) presented the numerical results of flow in a channel with slit rectangular ribs mounted on one channel wall. They observed two critical ranges of the open area ratio. There is no primary recirculation zone for the open area ratio above 44% and the perforated ribs act like the impermeable ribs for the open area ratio below 10%. Buchlin (2002) presented an experimental study of convective heat transfer in a channel with perforated rib arrangements, i.e. hole type, column type and chevron type using infrared thermography. The flow through the perforation was observed to interact with the recirculation bubble and remove the hot spot occurring behind the solid type rib. The perforation increases the local heat transfer enhancement by a factor of about 3.

Panigrahi and Tariq (2003) investigated the heat transfer and pressure penalty behind the surface mounted slit rib with different open area ratios and observed higher heat transfer for the slit rib compared to the solid rib for the open area ratio less than 30% with simultaneous reduction in pressure penalty compared to the solid rib. Tariq et al. (2004) reported the detailed flow and heat transfer behind slit rib of different open area ratio using liquid crystal thermography, hot wire anemometry, cold wire anemometry and flow visualization. They showed the interaction between the reattaching flow past the rib with the flow through the slit to successfully modify the near wall and wake region mean flow and fluctuation. Tariq (2004) compared the heat transfer and pressure drop of permeable rib arrays, i.e. slit rib, split-slit rib and inclined split-slit rib mounted on the bottom wall of a rectangular channel using liquid crystal thermography. The inclined split-slit rib array was observed to be most effective with about 22%

increase in average heat transfer and 12% drop in pressure penalty compared to the solid rib array. Panigrahi and Acharya (2004) used active acoustic excitation to study the effect of single tone and two harmonically related tones with different phase differences on the shear layer growth behind a surface mounted square solid rib. The fundamental excitation has highest shear layer growth among all single mode excitations and two-frequency excitation has comparable growth with weak dependency on phase difference. Panigrahi and Acharya (2005) presented the large scale and small scale turbulence contributions from pattern recognition technique and quadrant analysis of the flow over a surface mounted square rib under fundamental excitation. They reported the correlation between the non-Gaussian flow statistics with the ejection motion. Dutta and Hossain (2005) presented the heat transfer characteristics and associated friction head loss in a rectangular channel with perforated inclined baffles. The inclined perforated baffles containing circular holes facilitate jet impingement toward the heat transfer surface. This offers combined benefit of three heat transfer augmentation techniques, i.e. ribs, channel inserts and impingement cooling.

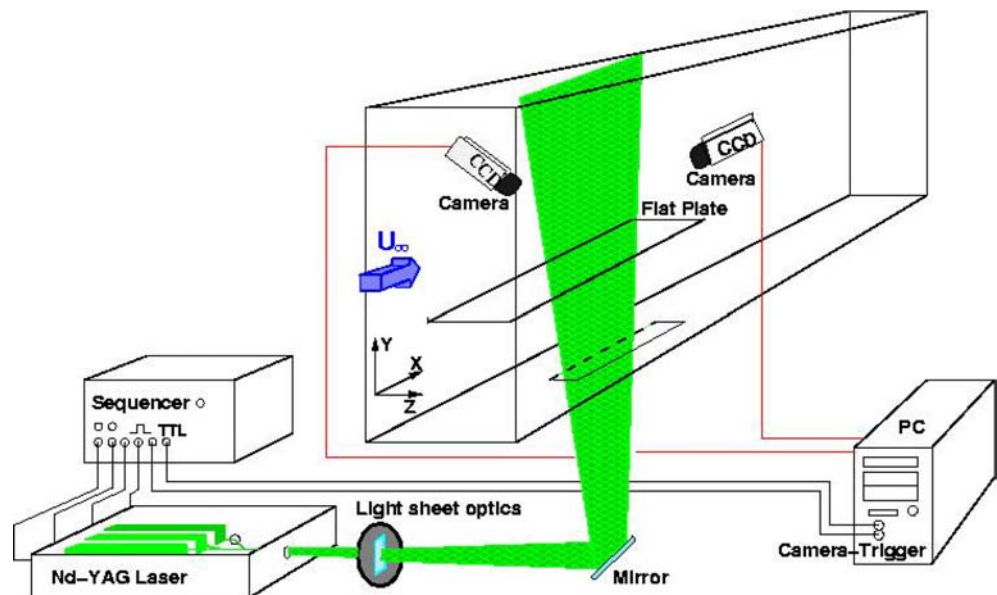
The above literature establishes the importance of passive and active flow control on flow past surface mounted ribs. The role played by production and manipulation of secondary vortical structures has been emphasized. However, the detailed flow field investigation of these flows is limited. The better understanding of these secondary flow structures and their interactions with the mean flow is expected to provide proper guidance in the design of rib geometries. Specific interest has been focused on the passive flow control by permeable ribs to explain the higher heat transfer and lower pressure penalty by these geometries. The axial vorticity (ω_x) is predominant in the delta wing type of turbulator, while the spanwise vorticity (ω_z) is strong in the normal rib type turbulator. The geometric modification, i.e. introduction

of slit and splitter in a solid rib (Fig. 2) is expected to combine the beneficial effect of both the delta wing and solid rib types of turbulator. Both the axial and streamwise vorticity is expected to be significant for the permeable rib turbulator geometry. Therefore, this work reports the vorticity, mean and fluctuating velocity field measurements in both streamwise (X - Y) and cross-stream (Y - Z) planes for different rib geometries, i.e. solid, slit, split-slit and inclined split-slit ribs. Both 2-C and 3-C stereo PIV measurements have been implemented and surface flow visualization has been used to add to the detailed flow structure understanding. The slit inclination and splitter effectiveness in generating additional vortical structures, i.e. horseshoe vortices and corner vortices have been established.

2 Experimental setup

The experiments have been carried out in the low turbulence wind tunnel of DLR Goettingen (Fig. 1). The test section is of $0.3 \times 1.5 \text{ m}^2$ cross-section and 6.25 m long. The air enters through a contraction cone (contraction ratio, 16:1), settling chamber of $5 \times 1.5 \text{ m}^2$ cross-section, honey comb and series of wire mesh. The average turbulence intensity of the wind tunnel is about 0.05%. A flat plate (Fig. 2) with a 6:1 elliptical leading edge (to prevent large scale boundary layer separation at the leading edge), 300 mm wide and 1,180 mm long has been mounted between the side walls of the wind tunnel as a test model. One sand paper of 10 mm width has been mounted at the leading edge of the flat plate and a second sand paper of 20 mm width has been mounted at a streamwise distance of 140 mm from the leading edge of the flat plate. A glass window has been mounted at the central bottom portion of the flat plate for the access of laser light sheet from below. The wooden portion of the flat

Fig. 1 The sketch of the experimental setup



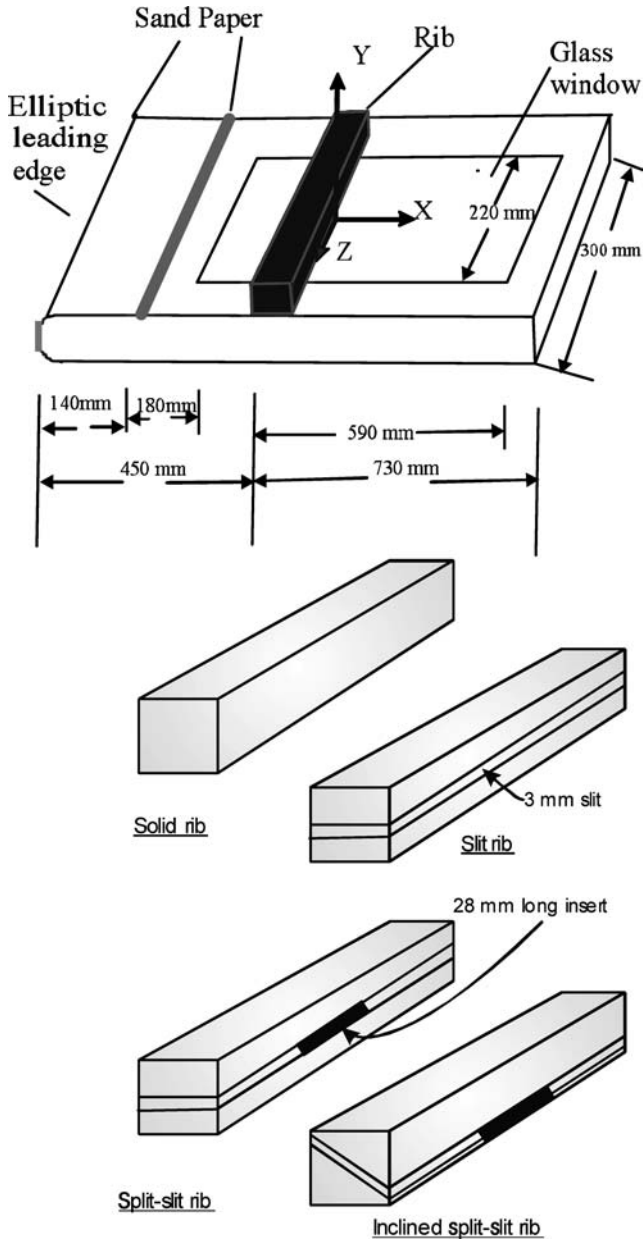


Fig. 2 The sketch of the flat plate, coordinate system and different rib turbulator geometries

plate, ribs and the remaining portion of the test section have been painted black to minimize the noise due to the reflection of laser light. The effect of ambient light on the measurement has been minimized by covering the test section with black screens.

The Nd:YAG laser system (Quantel) with an output energy of 180 mJ per pulse at a wavelength, $\lambda = 532$ nm has been used as light source. One biconcave lens ($f = -150$ mm), one biconvex lens ($f = 300$ mm), one cylindrical lens ($f = 40$ mm) and four mirrors have been used to generate a light sheet of about 1.0–1.5 mm thickness. The synchronization between the laser light pulses and the camera has been accomplished by the TTL pulses from the synchronizer (PIVTEC). The

cylindrical lens and the mirror positions are adjusted for controlling the light sheet position and its orientation with respect to the mean flow (stream wise or cross-stream). Two PCO Sencicam cameras (Kelheim, Germany) of 1,280×1,024 pixels with Zeiss (Jena, Germany) makro planar objectives (f -number = 2.8, $f = 100$ mm) have been used for image acquisition.

The stereo PIV system has been configured based on the angular lens displacement with tilted back plane (Scheimpflug condition). The calibration grid images from both the cameras have been reconstructed to the object plane based on a back-projection algorithm. To measure the misalignment between the light sheet and the calibration grid, a residual alignment is carried out by cross correlating the particle images captured at the same time from both cameras. For this procedure, the focus of the laser light sheet is moved close to the measurement region to obtain narrow correlation peaks and high accuracy. After the completion of residual alignment, the light sheet thickness in the measurement region is increased to about 1.5 mm for accurate capturing of the out of plane velocity. The reconstructed calibration coefficients for each camera are used to calculate the planar velocity vector field for the respective cameras. The 3-C velocity field has been determined from the two planar velocity vector fields on the basis of perspective projection assuming geometric imaging.

A Laskin nozzle has been used to introduce the seeding at the entrance of the wind tunnel settling chamber. As tracer particles, diethylhexylsebacate (DEHS) supplied by Palas has been used. The mean tracer particle size is 1 μm (Kahler et al. 2002). The seeding generator is switched off during the data acquisition to eliminate any influence of external disturbance on the wind tunnel background turbulence due to the blowing of the compressed air through the seeding generator. The seeding density is mostly sufficient after running the seed generator for few minutes due to the recirculation of ambient room air. The quality of seeding density during the image acquisition is continuously monitored by online computer display.

The PIV measurements have been carried out both in streamwise (X – Y) and cross-stream planes (Y – Z). The different measurement planes for the present study have been shown in Fig. 3. The measurements in the streamwise and cross-stream planes have been obtained using 2-C PIV and 3-C stereo PIV, respectively. The measurements in the streamwise plane (X – Y) have been obtained in the centre of the tunnel, i.e. at $Z/h = 0$. The measurement in the cross-stream planes (Y – Z) is also centred about $Z/h = 0$ location. The measurement planes and techniques have been decided to obtain maximum flow details with due consideration to the optical access for camera and light sheet. The near wall measurements downstream of the rib turbulators (measurement zones 4–8) have been acquired with highest spatial resolution to resolve small length scale fluctuations in the flow. The PIV image acquisition parameters for different

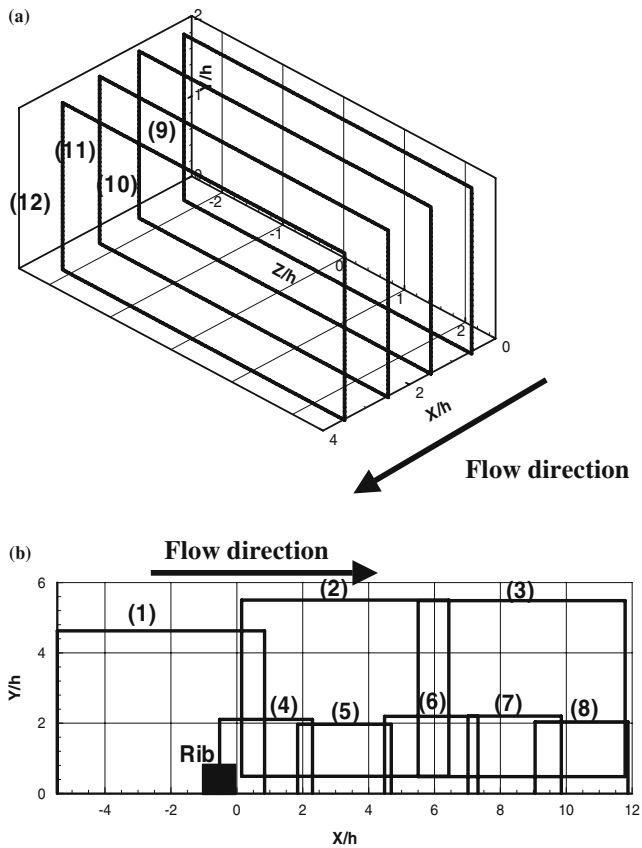


Fig. 3 The measurement zones in the **a** cross-stream and **b** streamwise plane

measurement zones have been compiled in Table 1. The cross correlation coefficient during PIV processing is lower inside the shear layer region compared to that inside the free stream and recirculation region due to high velocity gradient. The laser pulse separation time has been adjusted to optimize the maximum correlation value in the shear layer region. The typical correlation value was within 0.2–0.8, the lowest values being observed in the high shear region. The time separation between the two laser pulses is varied in the range of 60–90 μs . The absolute value of dynamic range during measurement is typically between 0.5 and 15.5 pixels. The frequency of image pair acquisition is 3.3 Hz. For the calculation of mean and fluctuating velocity field statistics, 1,200 image pairs have been acquired for each measurement zone.

Different rib turbulator geometries studied in this work are presented in Fig. 2. The ribs are made out of steel with sharp edges having a square cross section ($15 \times 15 \text{ mm}^2$) and spanning the total spanwise length (300 mm) of the test section. For the slit rib, there is a through slit at the symmetry line with a thickness equal to 3 mm leading to an open area ratio (ratio of the projected dimension of the slit to that of the rib) equal to 20%. A splitter of $28 \times 3 \text{ mm}^2$ cross-section is introduced at the centre of the slit for the split-slit rib and inclined split-slit rib. For the inclined split-slit rib, the slit is inclined at about 62° from the upstream top rib corner to the downstream bottom corner of the rib. The inclined slit at the downstream rib edge is located at 2 mm from the bottom surface.

Mixture of petrol and fiesta-fluo tracer (Gelb T-7, no: Lauco 4568) supplied by Fa Lauger & Co has been used for oil film visualization. The oil film was applied on the test surface behind the rib by means of a roller-coating device. The flow at Reynolds number equal to 19048 was subsequently introduced by initiating the flow through the tunnel. A steady-state surface pattern emerges and a digital camera has been used to acquire and store the surface visualization images.

3 Data reduction and presentation

3.1 PIV processing

The PIV image processing parameters for different measurement zones have been compiled in Table 2. The raw PIV images are high pass filtered (kernel size = 5 pixel) prior to the PIV cross correlation calculation. The background as seen by the two cameras for stereo PIV measurements are different from each other and it is not possible to completely eliminate the background light contribution due to the angular arrangement of the cameras. Therefore, an additional background subtraction of each camera image has been carried out during pre-processing stage for the measurement zones 9–12. The cross correlation scheme has been used for measuring the particle displacement in the measurement zones 1–8. For the stereo-PIV measurements (zones 9–12) double cross correlation, i.e. the product of two spatially separated correlation planes has been used to improve the cross correlation peak detection. The Whitaker sub-pixel correlation peak fit algorithm has been used for the

Table 1 PIV acquisition parameters for different measurement zones

	Zones 4–8	Zones 1–3	Zones 9–12
Object size	($42.6 \times 34 \text{ mm}^2$)	($95.5 \times 76.2 \text{ mm}^2$)	($71 \times 31 \text{ mm}^2$)
Image size	1,280 \times 1,024 pixels	1,280 \times 1,024 pixels	1,280 \times 1,024 pixels
Calibration	27 pixel/mm	13.5 pixel/mm	20 pixel/mm
Frequency (frame rate)	3.3 Hz	3.3 Hz	3.3 Hz
Number of samples	1,200	1,200	1,200
Pulse separation	70 μs	70 μs	90 μs
Light sheet thickness	$\approx 1 \text{ mm}$	$\approx 1 \text{ mm}$	$\approx 1.5 \text{ mm}$

Table 2 PIV processing parameters for different measurement zones

	Zones 4–8	Zones 1–3	Zones 9–12
Pre-processing	High pass filter (Kernel size = 5 pixels)	High pass filter (Kernel size = 5 pixels)	High pass filter (Kernel size = 5 pixels) Background subtraction
Correlation	Cross correlation	Cross correlation	Double cross correlation
Algorithm multigrid interrogation	Initial window size (64×64) Final window size (16×16)	Initial window size (64×64) Final window size (16×16)	Initial window size (128×128) Final window size (32×32)
Subpixel image shifting	B-spline interpolation (order 2)	B-spline interpolation (order 2)	B-spline interpolation (order 4)
Subpixel peak fit	Whitaker reconstruction	Whitaker reconstruction	Whitaker reconstruction
Window size	16×16	16×16	32×32
Overlap	50%	50%	50%
No. of vectors	159×127	159×127	91×40
Spatial resolution	0.54 mm	1.2 mm	1.6 mm

fractional displacement estimation. Multi-grid correlation from an initial grid size to a final grid size has been implemented for local window shifting with sub-pixel image deformation (B-Spline interpolation) to improve the dynamic range and accuracy. The spurious vectors calculated based on the median filter and maximum displacement differences are less than 1%.

The error in the back-projection calculation, the error in Scheimpflug adjustment and the camera noise add to the uncertainty in the velocity field calculation. To assess the accuracy of the PIV implementation, the 3-C stereo PIV measurements have been repeated with 2-C PIV technique for a smooth surface flow. The stereo PIV measurements have been acquired with the light sheet aligned both in streamwise (X – Y) and spanwise (Y – Z) plane. The mean and rms u -velocity from the 2-C and 3-C PIV techniques have been compared in Fig. 4. The stereo measurement in streamwise (X – Y) plane reports the in-plane u -velocity and the stereo measurement in spanwise (Y – Z) plane reports the out-of-plane u -velocity. The mean velocity field shows a perfect match between 2-C and 3-C PIV implementation. This confirms the accuracy of the stereo PIV in resolving both the in-plane and out-of-plane component of velocity. The rms velocity in Fig. 4 also shows a reasonable match between different PIV implementations with the magnitude from stereo PIV measurements being lower than the 2-C PIV counterpart. This may be attributed to the lower resolution of stereo PIV measurements and therefore the flow length scales resolved by the stereo PIV measurements are less than that of the 2-C PIV. The rms statistics for above measurements have been obtained from using 1,000 PIV recordings. To reduce the unsteadiness in the fluctuating field measurements, the number of PIV recordings has been increased to 1,200 for subsequent measurements reported in this work.

3.2 Vortex identification parameters

The measurements for this study have been performed in both the spanwise (Y – Z) and streamwise (X – Y)

planes. Therefore, the vorticity in the streamwise direction (ω_x) and spanwise direction (ω_z) have been reported:

$$\omega_x = \left(\frac{\partial w}{\partial Y} - \frac{\partial v}{\partial Z} \right)$$

$$\omega_z = \left(\frac{\partial v}{\partial X} - \frac{\partial u}{\partial Y} \right)$$

The vorticity field cannot distinguish between the swirling motion associated with a vortex and shear present in a wall bounded flow. The negative λ_2 criterion suggested by Jeong and Hussain (1995) is successful in discriminating the swirling motion from the shearing motion. The λ_2 is the second largest eigen value of $\mathbf{S}^2 + \mathbf{\Omega}^2$, where \mathbf{S} and $\mathbf{\Omega}$ are the symmetric and antisymmetric components of the velocity gradient tensor. The 2-D simplification of the λ_2 criterion has been calculated in X and Z direction, respectively, using:

$$\lambda_{2-x} = \left(\frac{\partial w}{\partial Z} \right)^2 + \left(\frac{\partial v}{\partial Z} \right) \left(\frac{\partial w}{\partial Y} \right)$$

$$\lambda_{2-z} = \left(\frac{\partial u}{\partial X} \right)^2 + \left(\frac{\partial v}{\partial X} \right) \left(\frac{\partial u}{\partial Y} \right)$$

The second invariant of the velocity gradient tensor ($Q = 0.5 \times (\text{tr}(\mathbf{\Omega}\mathbf{\Omega}^t) - \text{tr}(\mathbf{S}\mathbf{S}^t))$) (Jeong and Hussain 1995) has also been calculated for the vortex identification. The large positive Q -values indicate vortex and negative values indicate straining. The 2-D simplification of the Q -value in X and Z direction has been calculated, respectively, from using:

$$Q_{2D-x} = -\frac{1}{2} \left(\frac{\partial w}{\partial Y} \right) \left(\frac{\partial v}{\partial Z} \right)$$

$$Q_{2D-z} = -\frac{1}{2} \left(\frac{\partial v}{\partial X} \right) \left(\frac{\partial u}{\partial Y} \right)$$

The differential velocity field from the experiment has been obtained using the Richardson's finite difference formula.

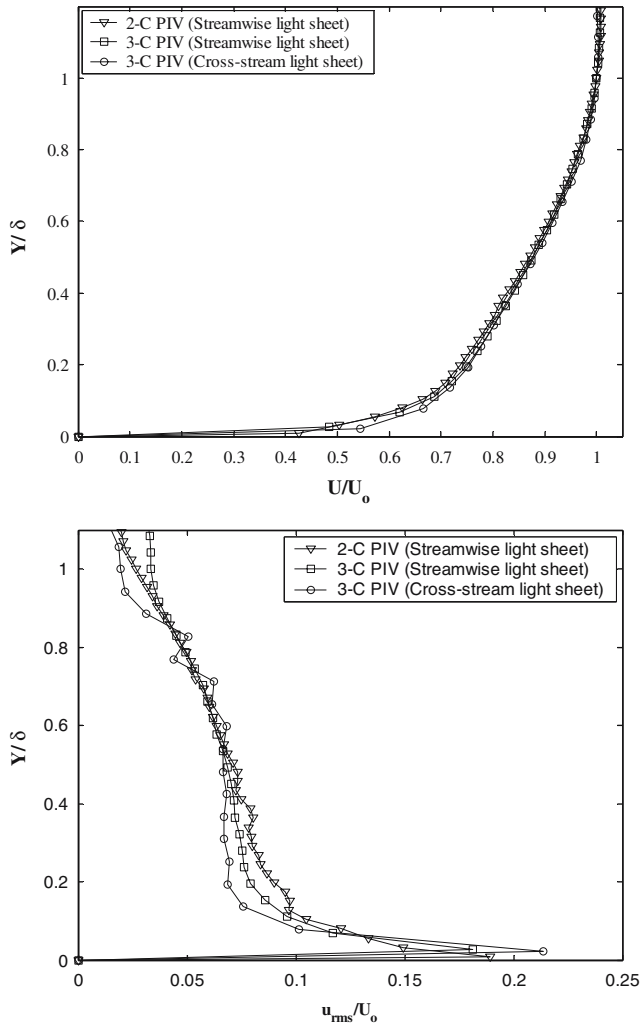


Fig. 4 The mean (*top*) and rms (*bottom*) u -velocity comparison for different implementations of the PIV technique, i.e. 2-C PIV, 3-C PIV with laser light sheet in streamwise and cross-stream plane

$$\frac{df}{d\eta} = \frac{-f_{i+2} + 8f_{i+1} - 8f_{i-1} + f_{i-2}}{12\eta} + O(\Delta\eta^3)$$

At the edge of the measurement region, the difference quantities have been calculated using forward and backward difference. The proper implementation of vorticity (ω), eigen value (λ_2) and second invariant of the velocity gradient tensor invariant (Q_{2D}) calculation has been verified using a numerically generated simulated velocity field consisting of two Oseen vortices superposed on shearing motion with $\tan h$ profile (Schram et al. 2004). The numerically calculated vorticity is identical to the analytical vorticity value of Oseen vortex. The $-\lambda_2$ and $+Q_{2D}$ quantities showed large positive values at the position of Oseen vortex core and slightly negative values at the localization of shear layer. The above observation supports the proper implementation and effectiveness of vortex identification parameters (ω , λ_2 , Q_{2D}).

4 Results and discussions

4.1 Incoming flow

The smooth wall flow at the streamwise X -location where the rib is mounted has been compared with the turbulent universal boundary layer profile ($U^+ = Y^+$ when $Y^+ < 5$, $U^+ = 5.0$ $Y^+ - 2.9$ when $Y^+ < 2.0$ and $U^+ = 2.44 \ln Y^+ + 5.0$, otherwise) in Fig. 5. The wall shear velocity (U_τ) has been obtained by plotting the mean velocity profile (U/U_o vs. $U_o Y/\nu$) and least square fitting the universal velocity profile in the region exhibiting clear semi-logarithmic relationship. The shear velocity (U_τ) is equal to 0.29 m/s. The reasonable match between the universal boundary layer profile and the experiment indicates the turbulent nature of the incoming flow approaching the surface mounted rib. The properties of this incoming flow boundary layer have been compiled in Table 3. The surface mounted rib is submerged inside the incoming turbulent boundary layer of shape factor equal to 1.6. The Reynolds number based on the momentum thickness of the incoming boundary layer and the rib height is equal to 695 and 5,538, respectively.

The streamwise velocity (u) field upstream of the rib for different rib geometries has been compared in Fig. 6. For the solid rib, the approaching boundary layer is deflected towards the top surface of the rib. A recirculation bubble of approximate size equal to the rib height extends upstream of the rib. For the slit rib, the flow through the slit is clearly visible with higher u -velocity at $Y/h \approx 0.5$ location. The overall size of the upstream recirculation bubble is smaller for the slit rib compared to that of the solid rib. For the split-slit rib higher u -velocity is also observed near the $Y/h = 0.5$

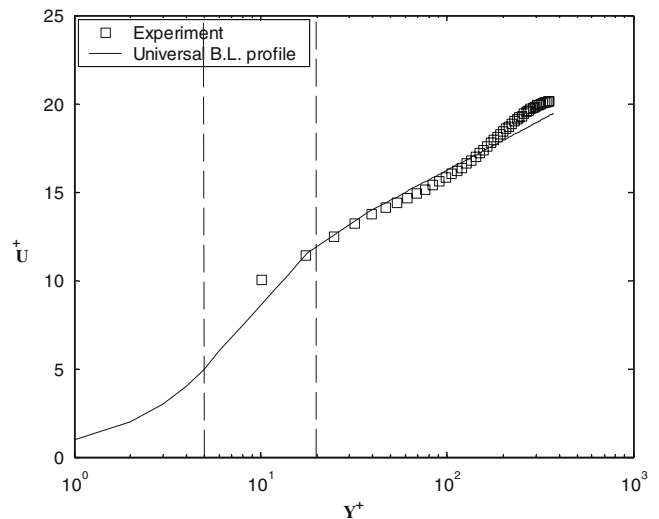


Fig. 5 The smooth-wall boundary layer profile in wall coordinate, where the rib is mounted. The universal B.L. profile, $U^+ = Y^+$ (when $Y^+ < 5$), $U^+ = 5.0$ $Y^+ - 2.9$ (when $Y^+ < 2.0$) and $U^+ = 2.44 \ln Y^+ + 5.0$ (otherwise) have been super-imposed for comparison

Table 3 The smooth surface boundary layer properties at the streamwise location (X) where the rib is mounted

δ (mm)	δ^* (mm)	θ (mm)	U_τ (m/s)	U_o (m/s)
15.3	2.86	1.758	0.29	5.8

location. However, the magnitude of the u -velocity for the split-slit rib is lower than that of the slit rib due to the presence of the splitter preventing through flow. The size of the maximum negative velocity region is higher for the split-slit rib compared to that of the slit rib. The higher u -velocity at about $Y/h=1.0$ location for the inclined split-slit rib indicates flow through the inclined slit. Overall, the presence of perforation inside the rib effects the upstream separating flow and hence

the separation process. The effect of these modifications on the flow structure at the downstream region of the permeable ribs have been presented and discussed in the following sections.

4.2 Surface flow visualization

The oil film visualization results for different rib geometries have been shown in Fig. 7. The nomenclature describing critical surface flow patterns, i.e. saddles (S) and focus (F) (Perry and Chong (1987)) have been marked on top of the images. The visualization image of the solid rib in Fig. 7 is quite similar to the visualization pictures of Martinuzzi and Tropea (1993). The first continuous line saddle immediately

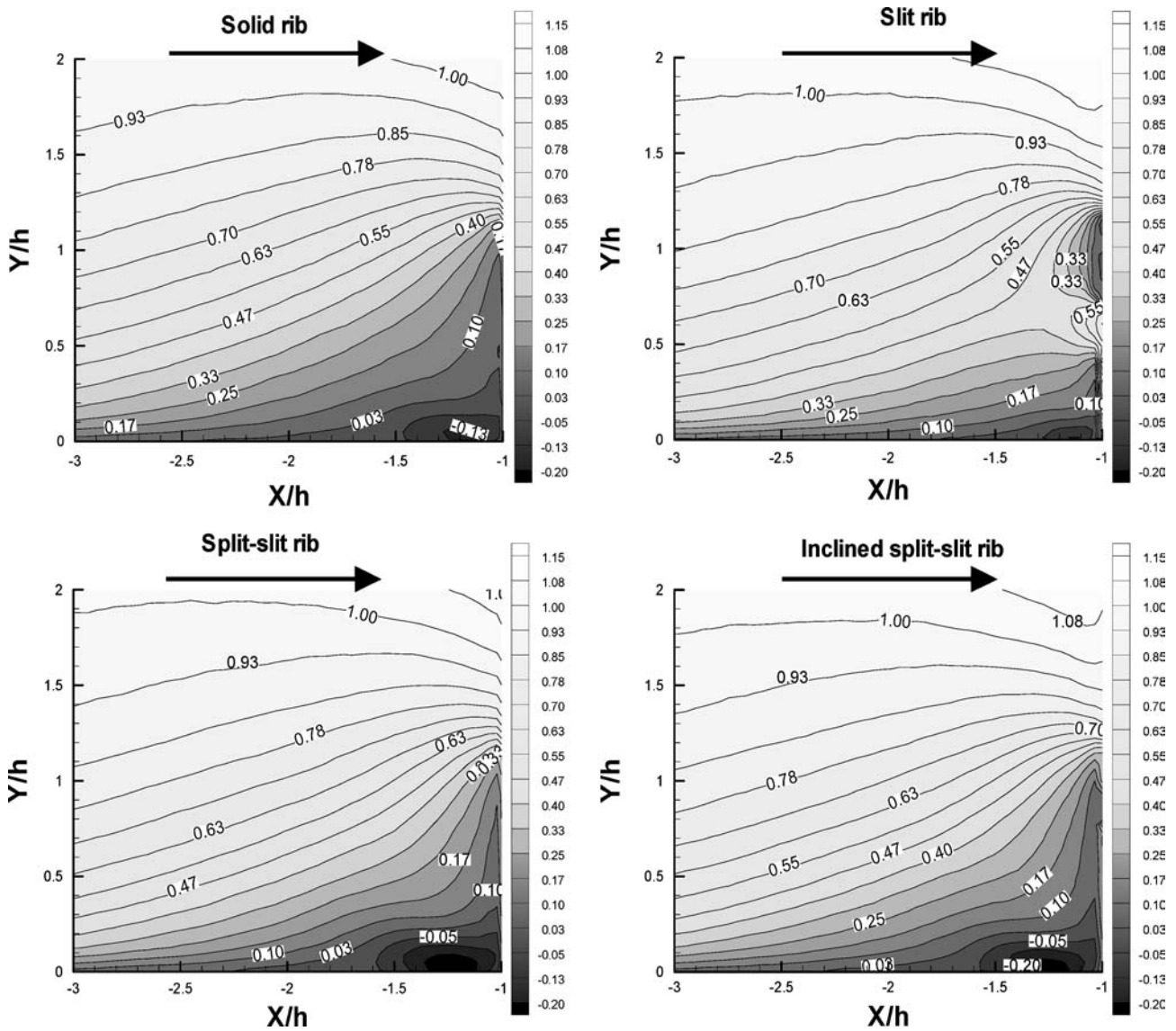
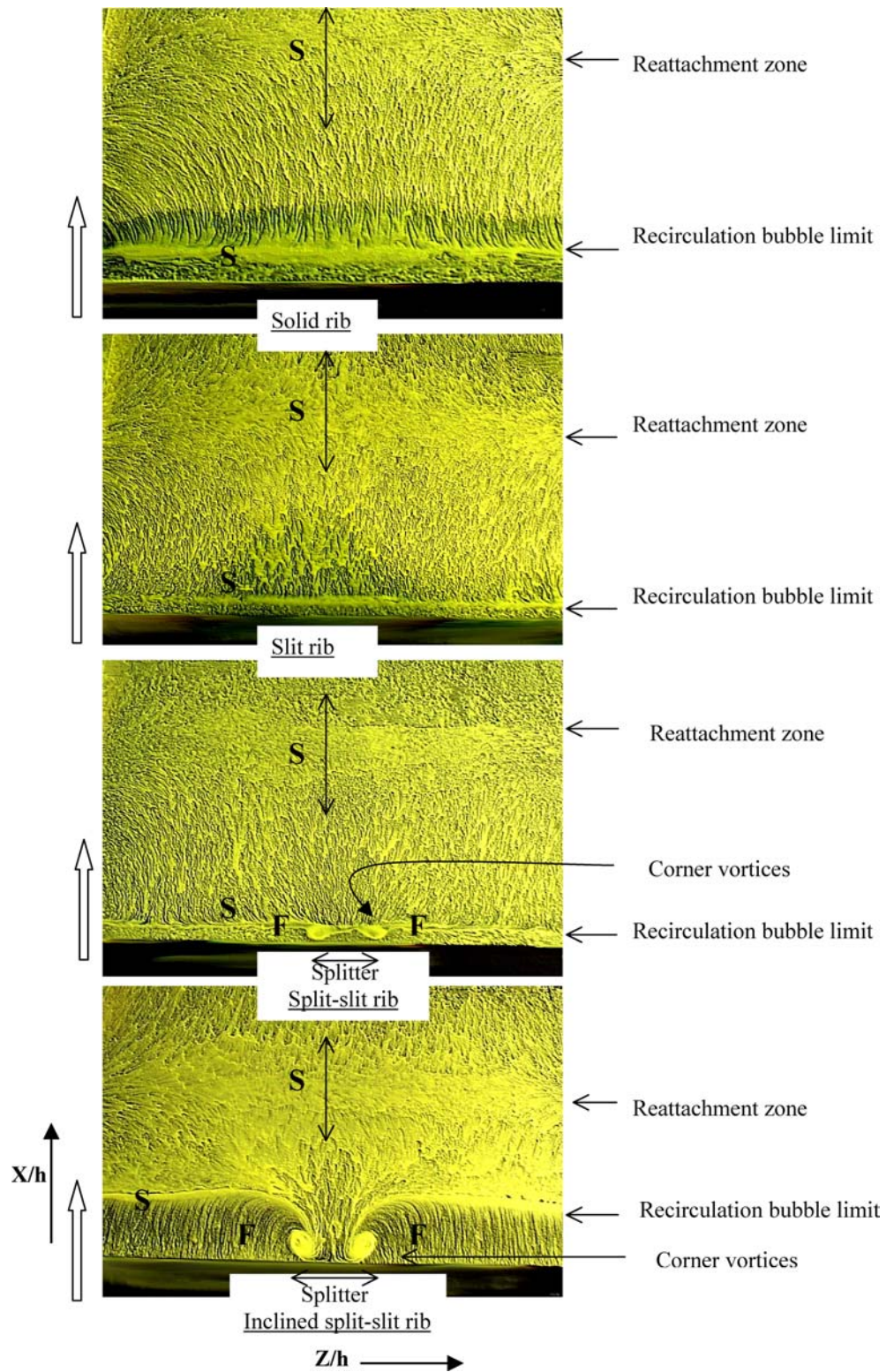


Fig. 6 Upstream streamwise velocity ($\langle u \rangle / U_o$) field at $Z/h=0$ plane for different rib geometries. The upstream edge of the rib extends from $X/h=-1; Y/h=0$ to $X/h=-1; Y/h=1$

Fig. 7 Surface visualization pictures behind different rib geometries



behind the rib with negligible streamwise velocity is the limiting line between the secondary vortex at the rib corner and the primary recirculation bubble. The second saddle line is located further downstream from the rib at the reattachment location. The visualization

image of the slit rib shows similar critical surface patterns as that of the solid rib. However, the reattachment region has moved closer towards the rib and the limiting line between the primary and secondary recirculation bubble is less distinct for the slit rib in

comparison to that of the solid rib. In addition to the presence of reattachment region and the limiting saddle line between the primary and secondary recirculation bubble, two vortices behind the splitter are seen for the split-slit rib in Fig. 7. These two vortices are located at the corner of the splitter and therefore have been termed as corner vortices. These two corner vortices can be construed similar as those seen behind a surface mounted cube (Martinuzzi and Tropea (1993)). However, the geometry and shape of the corner vortices for these two cases are not similar due to difference in the upstream boundary condition. The visualization image behind the inclined split-slit rib shows larger corner vortices compared to that of the split-slit rib and the film-like flow through the inclined slit is clearly visible at the downstream rib corner. The shape of the corner vortices behind the split-slit rib is similar to the stable foci seen in the surface visualization image of a missile shaped body (Perry and Chong (1987)). The corner vortices drag the fluid from the primary recirculation bubble towards the rib leading to significant reduction in reattachment length for the inclined split-slit rib. The strong flow through the inclined slit in the immediate downstream rib corner region (Fig. 7) is expected to alleviate the hot spot problem commonly seen behind the solid rib. The detailed mean flow and fluctuation statistics will be presented in the following sections to better explain the flow structures responsible in influencing the mean flow reattachment behaviour.

4.3 Reattachment length

Near the reattachment region, the flow approaches the bottom wall from a near normal direction and splits along the solid boundary. The reattachment length from the PIV measurements is obtained by investigating the sign of the near wall u -velocity. The reattachment length from the rearward face of the rib is determined as the location at which the u -velocity reverses its sign from negative to positive velocity. It is also further verified

that the change in sign of the velocity is a continuous phenomenon and any isolated change in the velocity sign due to possible noise effect is not considered as a valid reattachment point. The nearest measurement location from the wall being located at 0.27 mm from the bottom wall, the calculation of reattachment length can be considered to be sufficiently accurate with maximum error equal to 0.5 mm ($\Delta X_R/h=3.3\%$). The reattachment length was also obtained from the flow visualization images (Fig. 7). The central location of the reattachment zone from the downstream rib face was measured by a scale. Considering the dependency on visual identification of the reattachment point, the error in the reattachment length calculation is higher, i.e. about 2 mm ($\Delta X_R/h=13\%$).

The reattachment length calculated from the PIV measurements and the flow visualization images have been compared in Table 4. The reattachment lengths obtained from both techniques are within 7% of each other. The reattachment lengths obtained from previous studies have also been included in Table 4 for comparison. The reattachment length for the slit rib from this work is within 10% of the liquid crystal results from Tariq et al. (2004). The reattachment length for the solid rib is about 15% higher than the values reported in literature (Faramarzi and Logan 1991; Liou et al. 1990; Sparrow and Tao 1983). The higher reattachment length value observed for the solid rib in this work can be attributed to the difference in channel aspect ratio and the measurement uncertainty.

Overall, the reattachment lengths of the permeable ribs are smaller compared to the solid rib (Table 4). The drop in reattachment length is highest, i.e. about 41% for the inclined split-slit rib. This significant drop in reattachment length is very promising from flow management point of view. Tariq (2004) observed 23% higher heat transfer for the inclined split-slit rib compared to the solid rib. The drop in the primary recirculation bubble size, i.e. the low mixing region leads to enhancement in average heat transfer and mixing.

Table 4 The reattachment length (X_R/h) for different rib turbulators and comparison with literature

Classification	Reference	Technique	Reynolds no. (Re_h)	Pitch/height (P/h)	Reattachment length (X_R/h)
Solid rib	Present	PIV	5,538	∞	10.5
		Visualization	19,048		10.8
Slit rib	Present	PIV	5,538		8.2
		Visualization	19,048		8.6
Split-slit rib	Present	PIV	5,538		8.0
		Visualization	19,048		8.5
Inclined split-slit rib	Present	PIV	5,538		6.2
		Visualization	19,048		6.7
Solid ribSlit rib	Tariq et al. (2004)	Liquid crystal	2,480	∞	9.0
		Thermography			9.0
Solid rib	Faramarzi and Logan (1991)	Pressure and flow visualization	6,400 and 11,300	∞	9.1
Solid rib	Liou et al. (1990)	Laser Doppler velocimetry	4,546	70	8.9
Solid rib	Sparrow and Tao (1983)	Naphthalene sublimation technique	2,879	36.6	8.5

4.4 Mean flow

4.4.1 Streamwise plane

The magnitude of the normalized average velocity field ($\langle V \rangle / U_o$) behind the rib in the streamwise direction (X) at $Z/h=0$ plane and the corresponding streamline ($\langle \Psi \rangle$) topology for different rib geometries have been compared in Figs. 8 and 9, respectively. The primary recirculation bubble and the shear layer are separated from each other by a primary separation streamline with zero velocity (dark zone in Fig. 8). The middle of this dark zone at the wall surface, i.e. at $Y/h=0$ location corresponds to the reattachment point.

These reattachment locations are closely correlated to the reattachment results of Table 4. The primary separation streamline extends from the $Y/h \approx 1.0$ location to the wall ($Y/h \approx 0.0$) for the solid rib. In contrast, this separation streamline extends from the slit location ($Y/h \approx 0.5$) to a shorter reattachment point for the slit rib. The combined effect of smaller reattachment length and smaller cross-stream (Y) extent of the separation streamline leads to a smaller recirculation bubble for the slit rib compared to the solid rib. The flow through the slit is clearly visible from the high u -velocity magnitude at $Y/h \approx 0.5$ location. This flow is directed upwards and it interacts with the reattaching shear layer. Similar upward motion of the flow

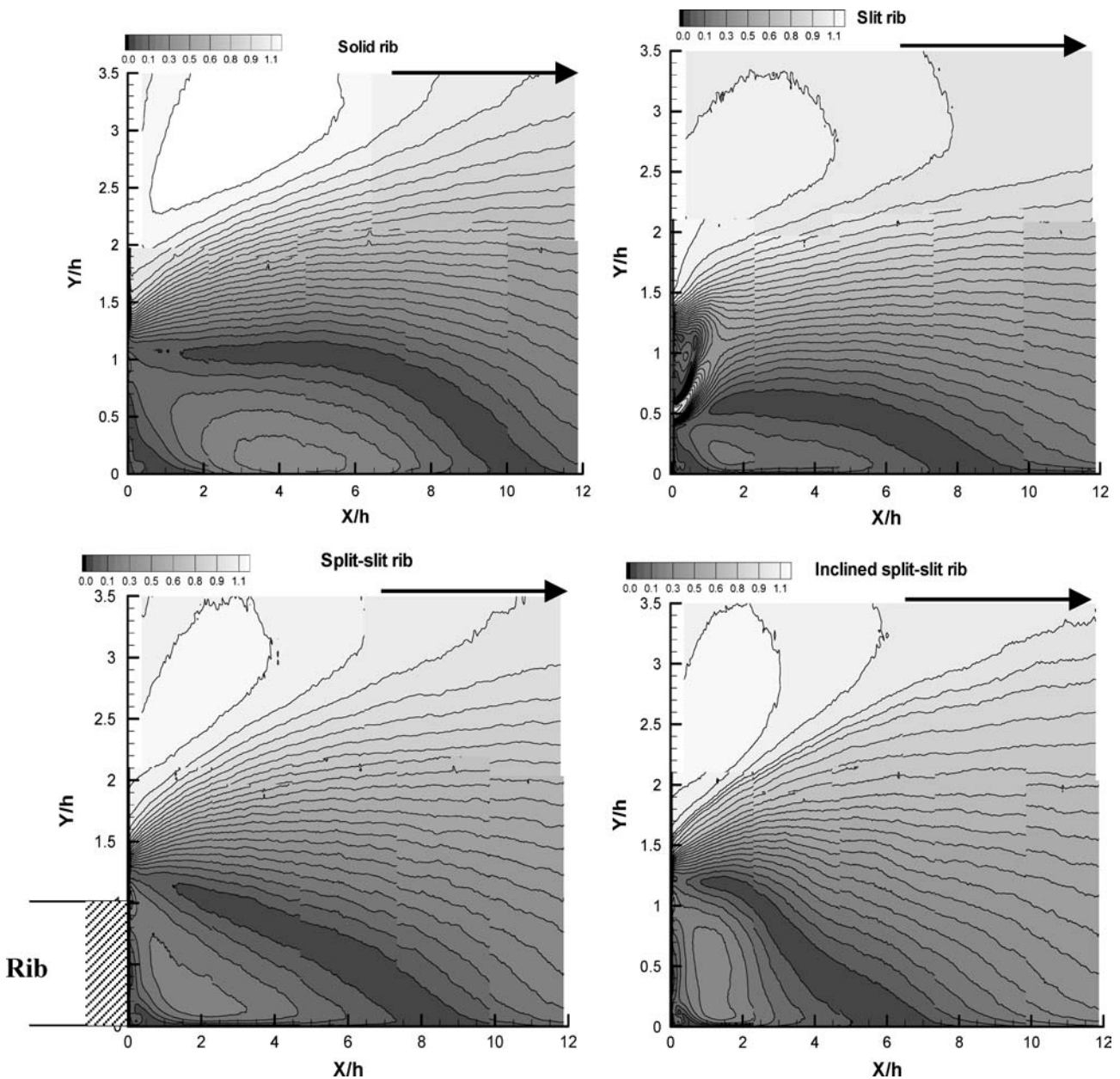


Fig. 8 The normalized average velocity field magnitude ($\langle V \rangle / U_o$) behind different rib geometries in the streamwise (X) direction

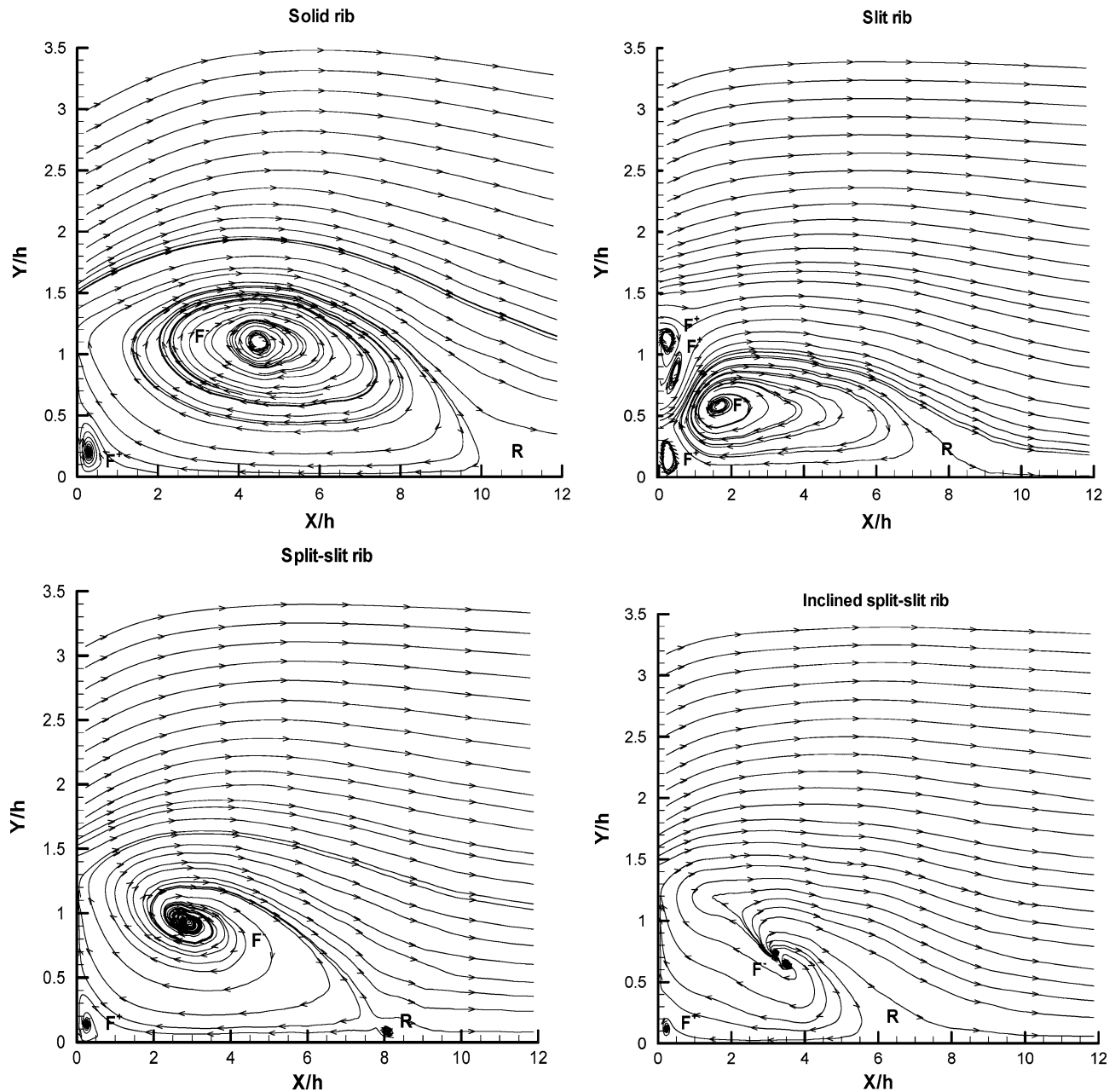


Fig. 9 The average streamline ($\langle \Psi \rangle$) plot behind different rib geometries in the streamwise (X) direction

through the slit has been observed in the visualization images of Tariq et al. (2004). The shape of the primary recirculation bubble is distinctly different for different rib geometries. The primary recirculation bubbles are oriented parallel to the bottom surface for the solid and slit ribs. In contrast, the recirculation bubbles behind the inclined split-slit and split-slit ribs are oriented at an angle to the bottom surface with greater cross-stream extent (Y/h) than its streamwise dimension. This indicates greater vertical momentum transport (v -velocity) inside the recirculation bubble for the split-slit and inclined split-slit ribs. A secondary separation streamline is also observed at the down-

stream rib corners for all rib geometries. This secondary separation line near the wall in Fig. 8 corresponds to the limiting saddle line seen near the rib corner in the visualization picture of Fig. 7. The secondary separation line in Fig. 8 is smaller and closer to the rib for the split-slit and inclined split-slit ribs compared to that of solid and slit ribs. The smaller secondary recirculation zone seen for the split-slit and inclined split-slit ribs can be attributed to the influence of corner vortices as observed in the flow visualization images of Fig. 7. Kostas et al. (2002) did observe both primary and secondary separation streamlines for a backward facing step.

The average streamline pattern in Fig. 9 shows definable time-averaged flow structure for all rib geometries. The primary recirculation bubble focus (Fig. 9) is located inside the low velocity zone (dark region of Fig. 8) for all rib geometries. The shape of the primary recirculation patterns is function of rib geometries and is distinctly different from each other. The recirculation pattern has symmetric shape for the solid rib similar to a limiting cycle. The compression in streamlines at the upstream of the focus indicates the stretching of the primary recirculation bubble of the slit rib in X -direction due to flow through the slit (Fig. 9). Two additional swirl patterns are observed at the top downstream corner of the slit rib ($Y/h \approx 1.0$). One swirl pattern originates from the mean flow and the second one originates from the flow through the slit. The recirculation patterns of the split-slit and inclined split-slit ribs look like a regular foci. The focus of the inclined split-slit rib looks like a skewed critical point possibly due to strong 3-D separation. A secondary swirl pattern at the bottom downstream rib corner below the secondary separation line (Fig. 8) is seen in Fig. 9 for all rib geometries. This has been confirmed as secondary corner vortex based on the results of coherent structures identifiers presented in later sections.

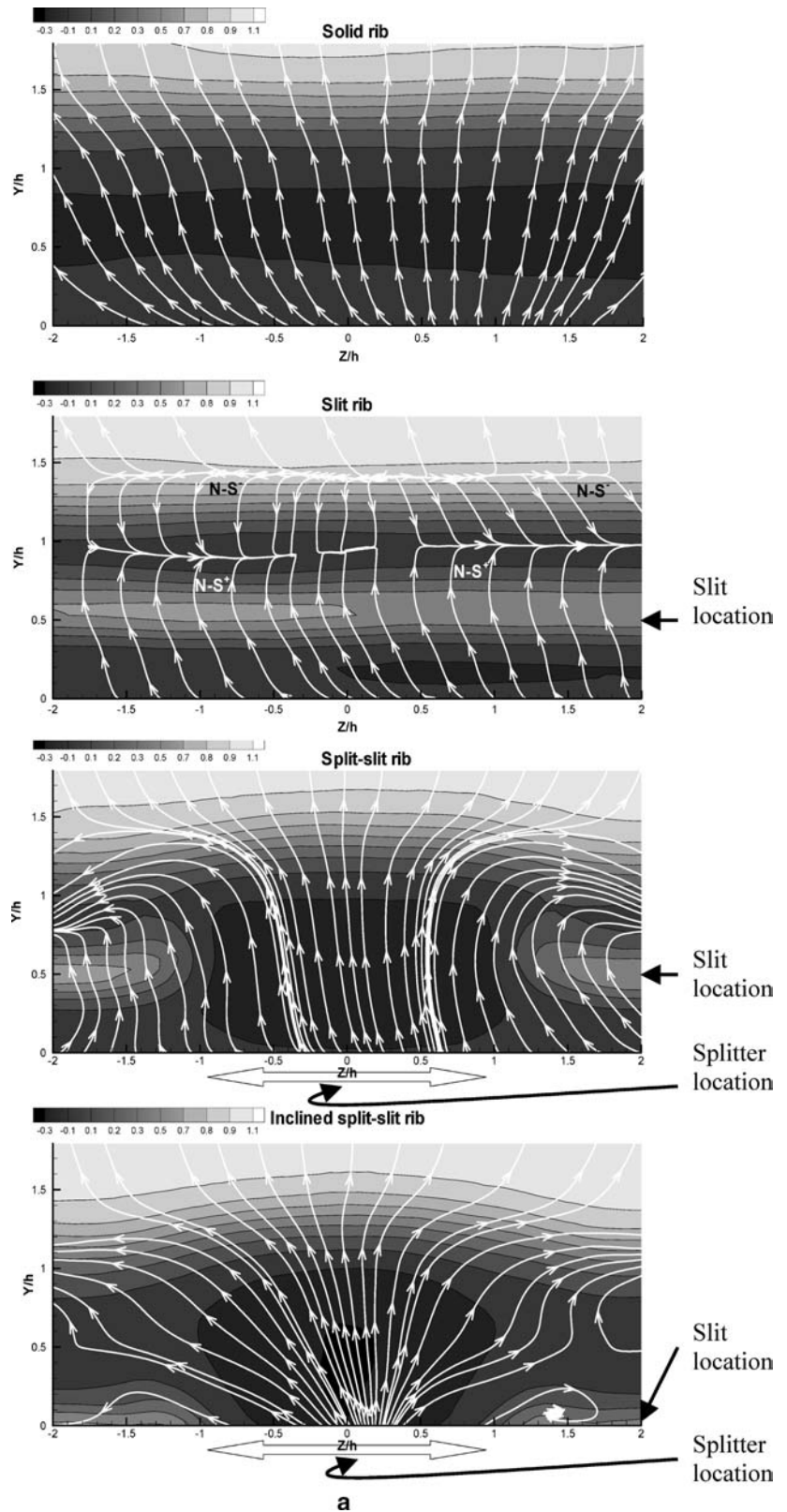
4.4.2 Cross-stream plane

The average streamwise velocity ($\langle u \rangle / U_o$) superposed on the average streamline (Ψ) calculated using the Y - Z component of velocity at different cross-stream planes ($X/h = 0.5, 1.5$ and 2.5) has been presented in Fig. 10. Figure 10a shows maximum negative u -velocity at about $Y/h = 0.6$ location for the solid rib ($X/h = 0.5$). The higher streamwise u -velocity observed in the near wall region is due to the presence of secondary recirculation bubble at the downstream rib corner. The streamlines in Y - Z plane for the solid rib (Fig. 10a) are directed towards the free stream region away from the bottom surface. This is in conformity with the average X - Y plane streamline topology of Fig. 9. The u -velocity distribution for the slit rib in Fig. 10a shows the presence of two zones with negative streamwise u -velocity. The first negative u -velocity region is located between the lower part of the slit and the bottom wall surface. The second negative u -velocity region is located between the top part of the slit and the free stream. Line node-saddle patterns similar to the degenerate critical points described in Perry and Chong (1987) are observed for the slit rib at this location. The bottom line node-saddle is stable receiving flow from the slit and from the upper corner recirculation bubble in Fig. 9. The top line node-saddle is unstable and supplies flow to the upper corner recirculation bubble and mean flow. It should be noted that the $X/h = 0.5$ location is immediately outside the three average vortical patterns seen near the downstream of the slit rib in Fig. 9. The upward motion of the

streamline in the near wall region seen in Fig. 10a is in conformity with the upward deflection of the flow through the slit seen in Fig. 8. The u -velocity distribution for the split-slit rib in Fig. 10a shows a negative velocity region behind the splitter located around $Z/h = 0$ location. The flow through the slit at $Y/h = 0.5$ around both sides of the splitter is evident from the higher u -velocity magnitude. Hence, the primary recirculation bubble shown in Fig. 9 at $Z/h = 0$ location has different cross-stream (Y) extent. The streamline behind the splitter moves from the bottom wall surface upwards and subsequently gets directed to both sides of the splitter in the spanwise (Z) direction (Fig. 10a). This flow pattern is in conformity with the flow towards the rib seen between the corner vortices in the visualization picture of Fig. 7. The flow dragged by the corner vortices from the recirculation bubble moves upward due to the obstruction provided by the splitter. The maximum negative u -velocity region of the inclined split-slit rib observed behind the splitter location (Fig. 10a) and its shape is different from that seen for the split-slit rib. The flow through the inclined slit is visible from the higher u -velocity magnitude in the near wall region, i.e. at about $Y/h = 0.1$ location. The streamline behind the inclined split-slit rib emerges upward from the bottom surface behind the splitter, which subsequently diverges and curves to both sides of the splitter (Fig. 10a). The flow through the inclined slit shows a small focus in the near-wall region indicating the swirling nature of flow through the slit.

Figure 10b shows the streamwise flow (u -velocity) superposed on the average streamline patterns at $X/h = 1.5$ location. The cross-stream (Y) extent of the negative velocity region for the solid rib is higher at $X/h = 1.5$ location compared to that at $X/h = 0.5$ (Fig. 10a). The positive u -velocity in the near wall region due to the presence of secondary recirculation bubble near the downstream rib corner is no more significant at $X/h = 1.5$ location. The negative u -velocity in Fig. 10b is due to the primary recirculation bubble. The u -velocity distribution for the slit rib in Fig. 10b shows continuous increase in the Y -direction with no discontinuity due to flow through the slit. This observation confirms the average velocity field results in Fig. 8. The cross-stream (Y) extent of the negative velocity region is smaller for the slit rib compared to the solid rib due to the smaller recirculation bubble size (see Figs. 8, 9). The streamline pattern of the slit rib shows upward motion away from the bottom surface with some sideward curvature in the near wall region. The u -velocity for the split-slit rib in Fig. 10b shows that the negative u -velocity zone (dark region) has grown symmetrically in the spanwise (Z) direction compared to that in Fig. 10a. The higher u -velocity flow through the slit around the splitter results in spanwise variation of the primary recirculation bubble. The streamlines are directed upwards in conformity with the X - Y plane velocity field results shown in Fig. 9. In the near wall region, the streamlines are

Fig. 10 The average streamline ($\langle \Psi \rangle$) in the Y - Z plane superposed on the contour of normalized out of plane streamwise velocity ($\langle u \rangle / U_o$) for different rib turbulators at the cross-stream plane: **a** $X/h=0.5$, **b** $X/h=1.5$, **c** $X/h=2.5$



curved towards the centre of the splitter from both sides. The negative recirculation region of the inclined split-slit rib does not grow in the spanwise (Z) direction

in the near wall region contrast to the behaviour of split-slit rib (Fig. 10b). The strong flow through the inclined slit is distinctly visible near the bottom wall in

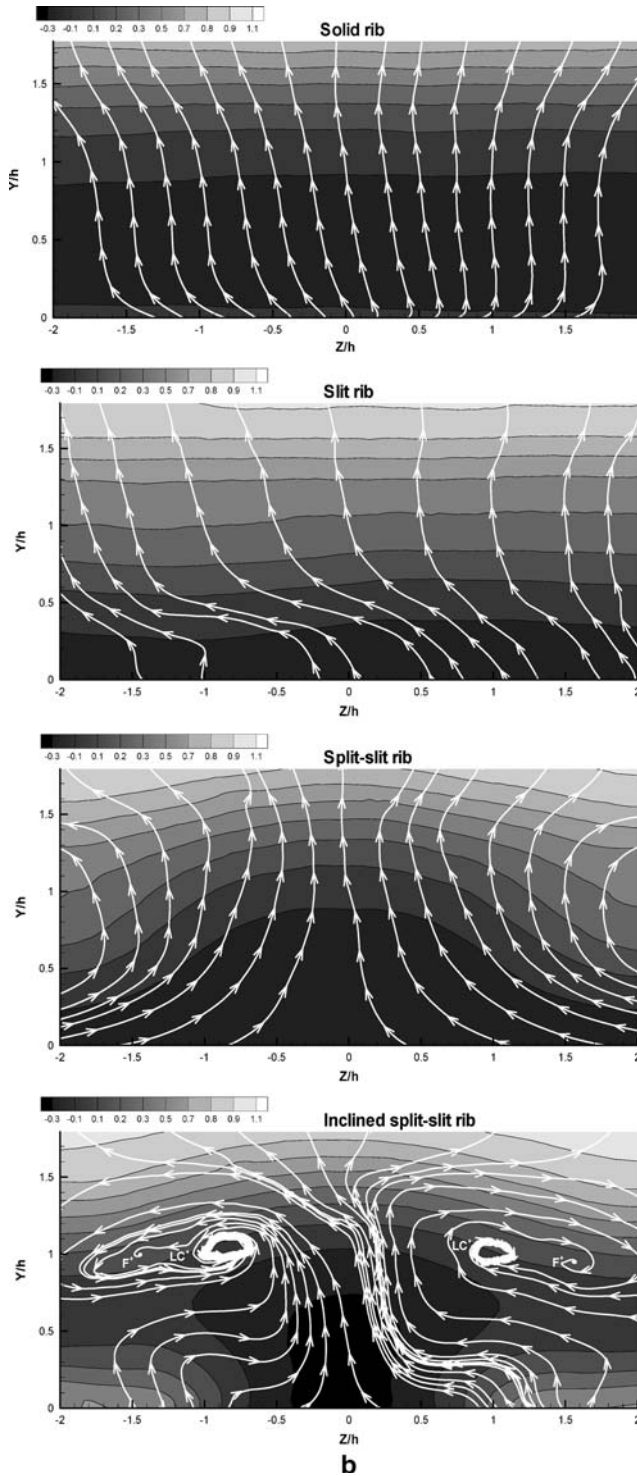


Fig. 10 (Contd.)

Fig. 10b. The shear layer due to the flow through the inclined slit has grown in the transverse (Y) direction. Two regular foci are located at both sides of the splitter (at about $Y/h = 1.0$), which emerge from the bottom test surface. These two vortices have similar orientation as the corner vortices seen in the flow visualization picture of Fig. 7.

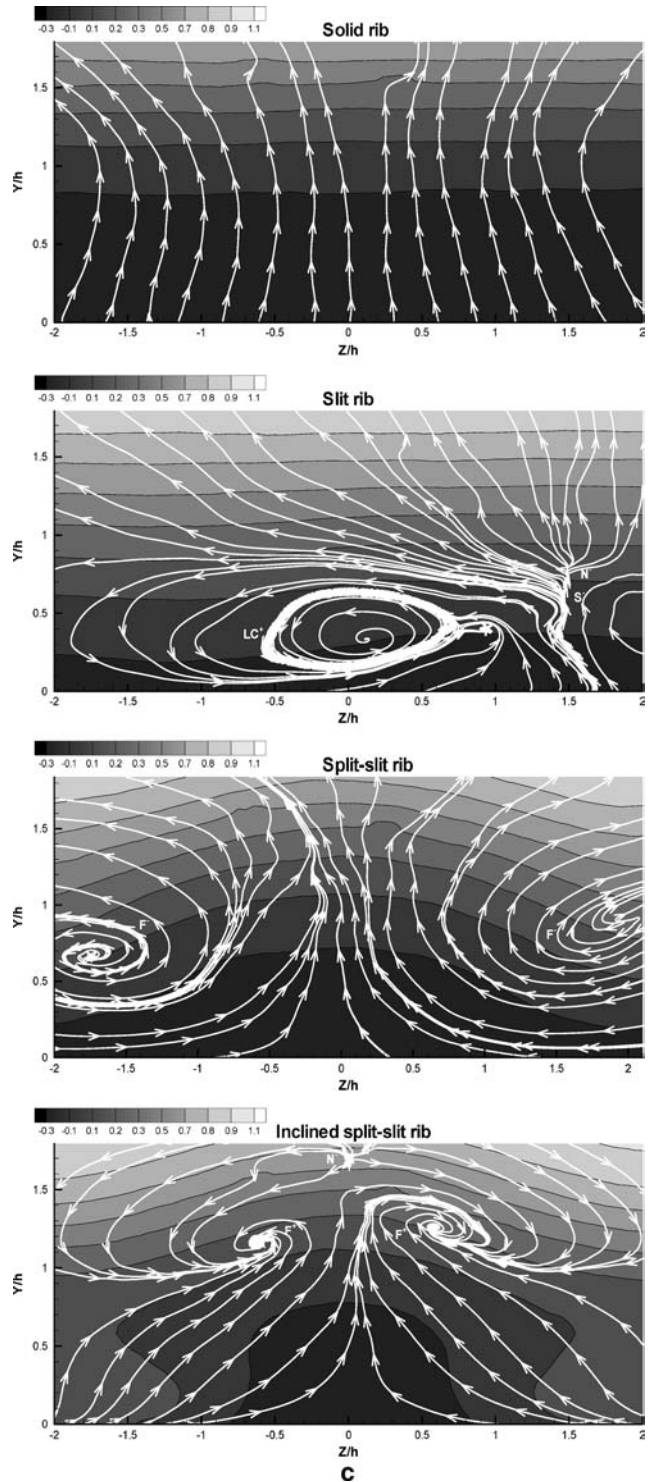


Fig. 10 (Contd.)

Figure 10c compares the streamwise u -velocity and average streamline at $X/h = 2.5$ location for different rib turbulators. The u -velocity distribution and streamline patterns in Fig. 10c for the solid rib are similar to those seen at the earlier location at $X/h = 1.5$ (Fig. 10b). This is also expected from the streamline plot in X - Y plane

(Fig. 9) as both the cross-stream locations ($X/h=1.5$ and 2.5) are at the same side of the primary recirculating bubble. The near wall curvature of the streamline seen in Fig. 10b for the slit rib leads to a swirling limit cycle pattern in Fig. 10c. It should be noted that $X/h=2.5$ location for the slit rib is at the downstream of the primary recirculation bubble foci seen in the X - Y plane (Fig. 9). A separate free-slip node and saddle direct flow towards the free stream for the slit rib. The u -velocity distribution for the split-slit rib in Fig. 10c shows similar distribution as seen in the earlier location, i.e. at $X/h=1.5$ with the size of the negative velocity region reducing in the cross-stream (Y) direction due to the downward motion of the reattaching shear layer. The sideward curvature of the streamlines seen in the earlier streamwise location (Fig. 10b) leads to two regular foci in Fig. 10c at both sides of the splitter. The u -velocity of the inclined split-slit rib in Fig. 10c shows significant value in the near wall region. The recirculation bubble has not grown in the spanwise (Z) direction compared to the earlier $X/h=1.5$ location. The symmetric primary recirculation bubble with Y -extent of about half the rib height is located at the centre region behind the inclined split-slit rib. The focus seen at $X/h\approx 1.5$ location in Fig. 10b is also observed in Fig. 10c. An additional free-slip star node is present at $Y/h\approx 1.6$ location directing flow towards the foci.

Overall, different critical flow patterns, i.e. nodes, saddles and foci are observed in the cross stream plane behind the permeable ribs contrast to the solid rib. These secondary flow structures are responsible for drop in reattachment length of the permeable ribs compared to the solid rib. The close correlation between the cross-duct motion and the size of the recirculation bubble reported by Iacovides et al. (2003) is in agreement with the above observation. Gao and Sunden (2004) also observed strong effects of the inclined ribs on the spanwise variation of the streamwise velocity component and attributed it to the presence of secondary flow leading to higher heat transfer.

4.5 Coherent structures

4.5.1 Streamwise plane

The non-dimensional average spanwise vorticity ($\omega_z h / U_o$) for different rib geometries have been presented in Fig. 11. To allow direct comparison, the minimum and incremental values of vorticity have been set to an identical value for all rib geometries. The vorticity is significant both inside the shear layer and in the near wall region. The near wall ($Y/h\approx 0.1$) vorticity changes its sign near the reattachment region. This is due to the motion of the impinging shear layer in opposite direction after reattachment. The X -location at which the near wall vorticity changes sign is within 7% of the reattachment length values reported in Table 4. The vorticity contour near the downstream rib corner

may be attributed to the secondary recirculation vortex. The location of the maximum vorticity inside the shear layer is not coincident with the foci of the primary recirculation bubble in Fig. 9. This is due to the lack of precise correspondence between the average streamline and vorticity. The influence of velocity gradient inside the shear layer effects the precise correlation between the vortex and the streamline pattern. The vorticity contour at the bottom rib corner coincides with the recirculating streamline pattern in Fig. 9. The success of the vorticity contour in identification of the secondary vortex is possible due to the absence of any significant shear. Jeong and Hussain (1995) showed that an inviscid streamwise vortex inside the homogeneous shear flow is not properly represented by vorticity contours. Rather the eigen value (λ_2) is successful in representing the vortex inside the shear flow.

To get further insight about the contribution from the rotational and shearing motion, the vorticity (ω_z), the 2-D approximation of eigen value (λ_{2-Z}) and velocity gradient tensor invariant (Q_{2D-Z}) at the immediate downstream location of the rib have been compared in Fig. 12. It may be clarified that the coherent structure identifiers (λ_{2-Z} and Q_{2D-Z}) should be looked at from qualitative perspective as the 2-D approximation for a 3-D flow has been used for their calculation. Both λ_{2-Z} and Q_{2D-Z} values are insignificant near the bottom wall for all rib geometries except at the downstream rib corner. Therefore, the vorticity at the bottom wall region (outside the corner vortex) should be attributed to the straining motion and not due to swirling motion. However, the high Q_{2D-Z} value at the downstream rib corner indicates significant vortical motion due to the secondary corner vortex. The significant λ_{2-Z} and Q_{2D-Z} values indicate that the vorticity inside reattaching shear layer near the top rib corner has significant rotational contribution. There is no single dominant large-scale vortical structure inside the shear layer similar to the corner vortex. The flow through the slit has significant swirling component, which interacts with the vortices present inside the reattaching shear layer.

The presence of secondary corner vortex at immediate downstream bottom corner of the rib is clearly demonstrated by the calculation of coherent structure identifiers (λ_{2-Z} and Q_{2D-Z}). This corner vortex is located between the rib and the primary recirculation bubble limit (Fig. 7). Martinuzzi and Tropea (1993) also proposed the presence of a corner vortex behind the solid rib based on their oil flow visualization study.

4.5.2 Cross-stream plane

The streamwise vorticity (ω_x) and the respective vortex identifiers (λ_{2-X} and Q_{2D-X}) for different rib geometries have been compared in Fig. 13 at $X/h=0.5$ location.

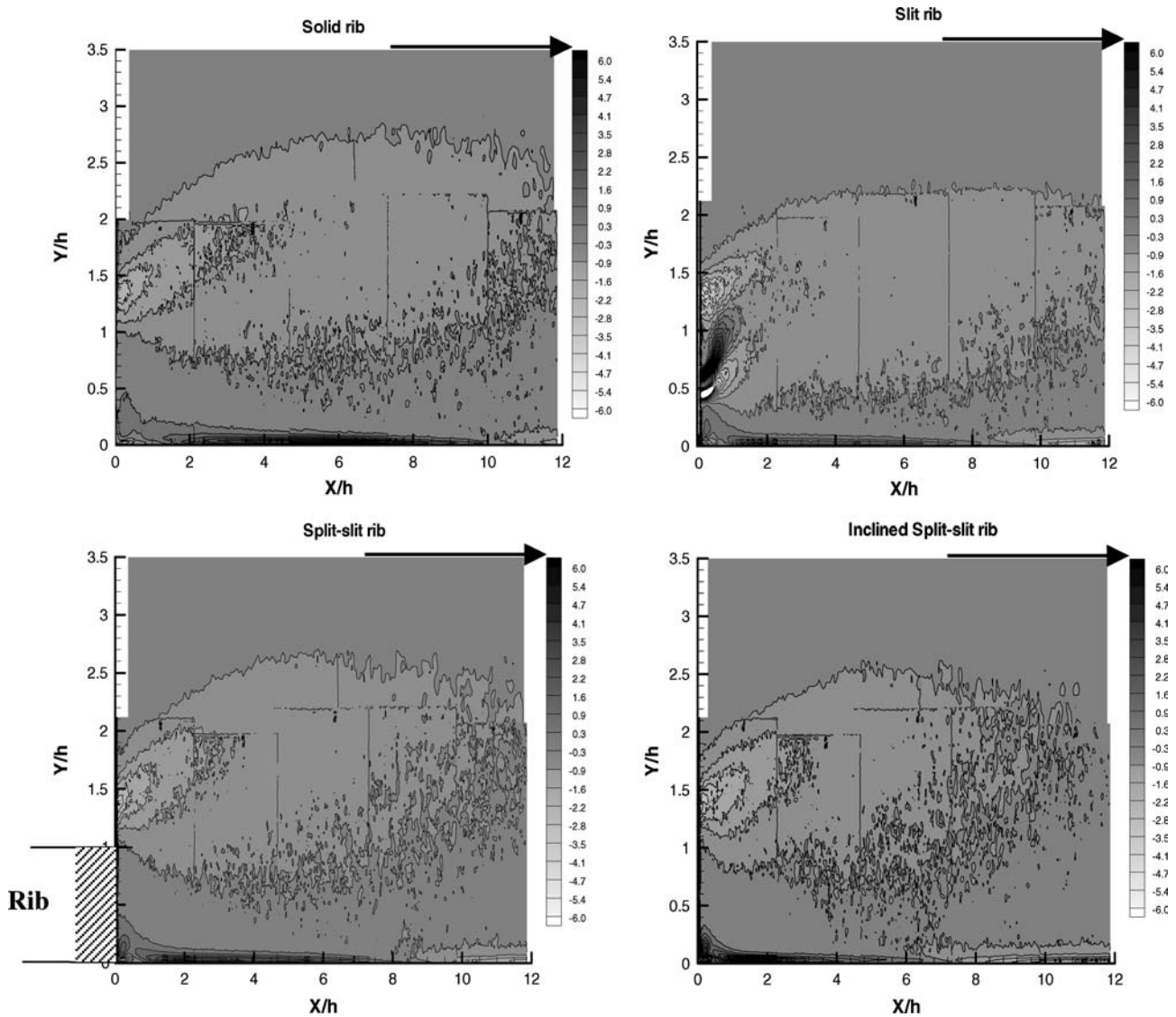


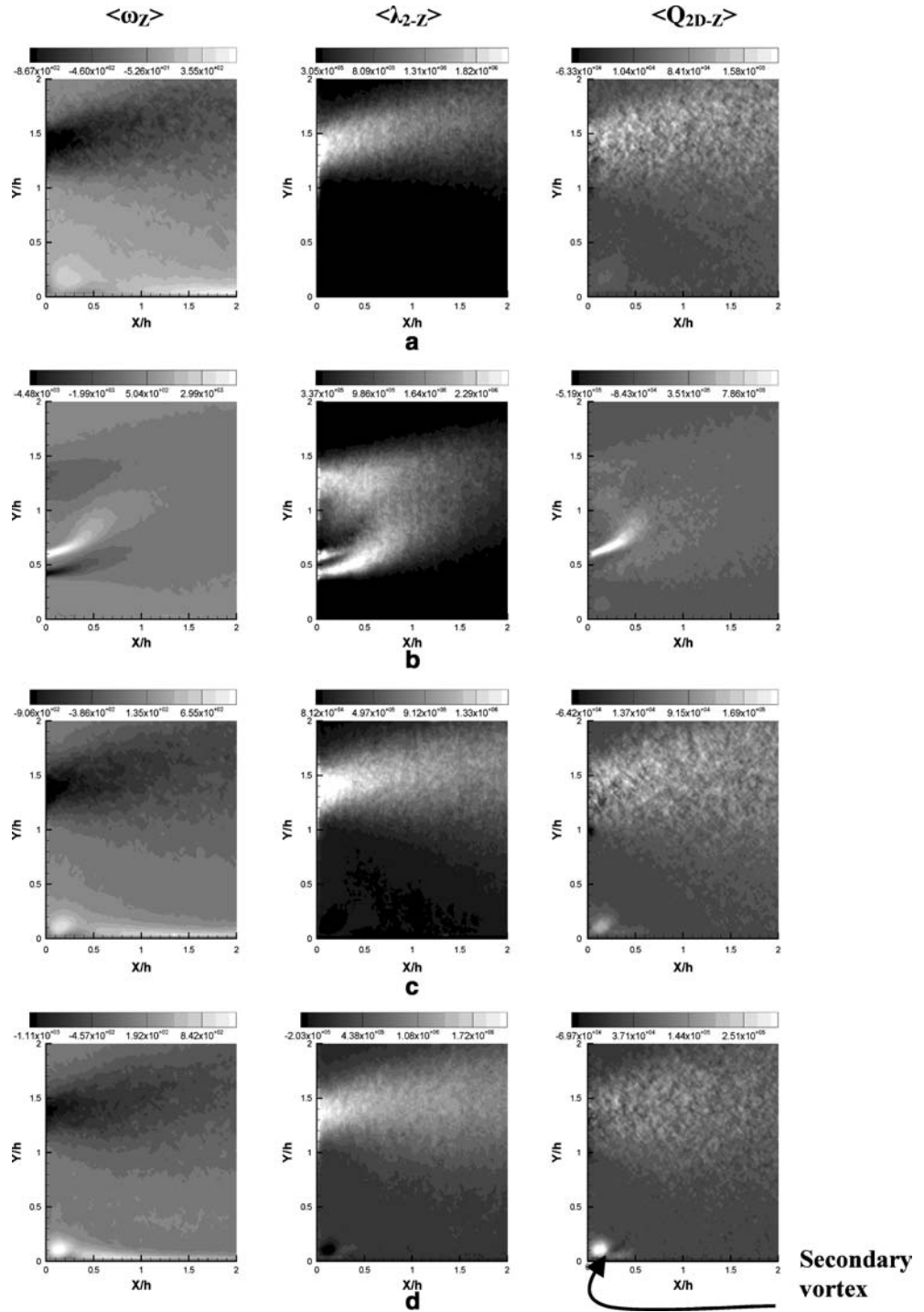
Fig. 11 The spanwise vorticity ($\omega_z h/U_o$) distribution behind different rib geometries in the streamwise (X) direction

The ω_X -vorticity for the solid rib is significant at similar location ($Y/h \approx 1.4$) where the spanwise vorticity (ω_Z) is significant in Fig. 12a. The ω_X -vorticity in Fig. 13b for the slit rib also shows high value at $Y/h \approx 0.5$ location similar to that of the ω_Z -vorticity in Fig. 12b. For the split-slit rib, strong spanwise (Z) variation of the streamwise vorticity (ω_X) is evident from Fig. 13c. In addition to significant ω_X -vorticity in the shear layer region ($Y/h \approx 1.25$), strong vorticity is observed near the slit location ($Y/h \approx 0.25-1$) at both sides of the splitter. Two opposite sign vorticity regions for the split-slit rib can be seen at about $Y/h \approx 0.5$ location, which corresponds to the central region of flow through the slit in Fig. 10a. Two additional strong vorticity regions of opposite sign can be observed at $Y/h \approx 0.8$ location. The vorticity inside the shear layer region ($Y/h \approx 1.0$) is high for the inclined split-slit rib (Fig. 13d). Two strong vorticity regions of opposite

sign are also observed at both sides of the splitter at $Y/h \approx 0.2$ location for the inclined split-slit rib. The λ_{2-X} and Q_{2D-X} values have been presented in Fig. 13 to distinguish the contribution from swirling and shearing motion towards the cross-stream vorticity (ω_X) distribution.

The eigen value (λ_{2-X}) and the Q_{2D-X} results in Fig. 13a show high value inside the shear layer ($Y/h = 1.0-1.6$) for the solid rib. This region is the high shear region in Fig. 10a having appreciable ω_X and ω_Z vorticity (Figs. 12a, 13a). This indicates the predominant swirling and shearing motion inside the shear layer of a solid rib. However, for the slit rib, the λ_{2-X} and Q_{2D-X} values are not significant at $Y/h \approx 0.5$ locations where the vorticity is significant (Fig. 13b). It indicates that the high vorticity around $Y/h \approx 0.5$ location is due to significant shear contribution. The λ_{2-X} and Q_{2D-X} values are significant for a wider zone in the

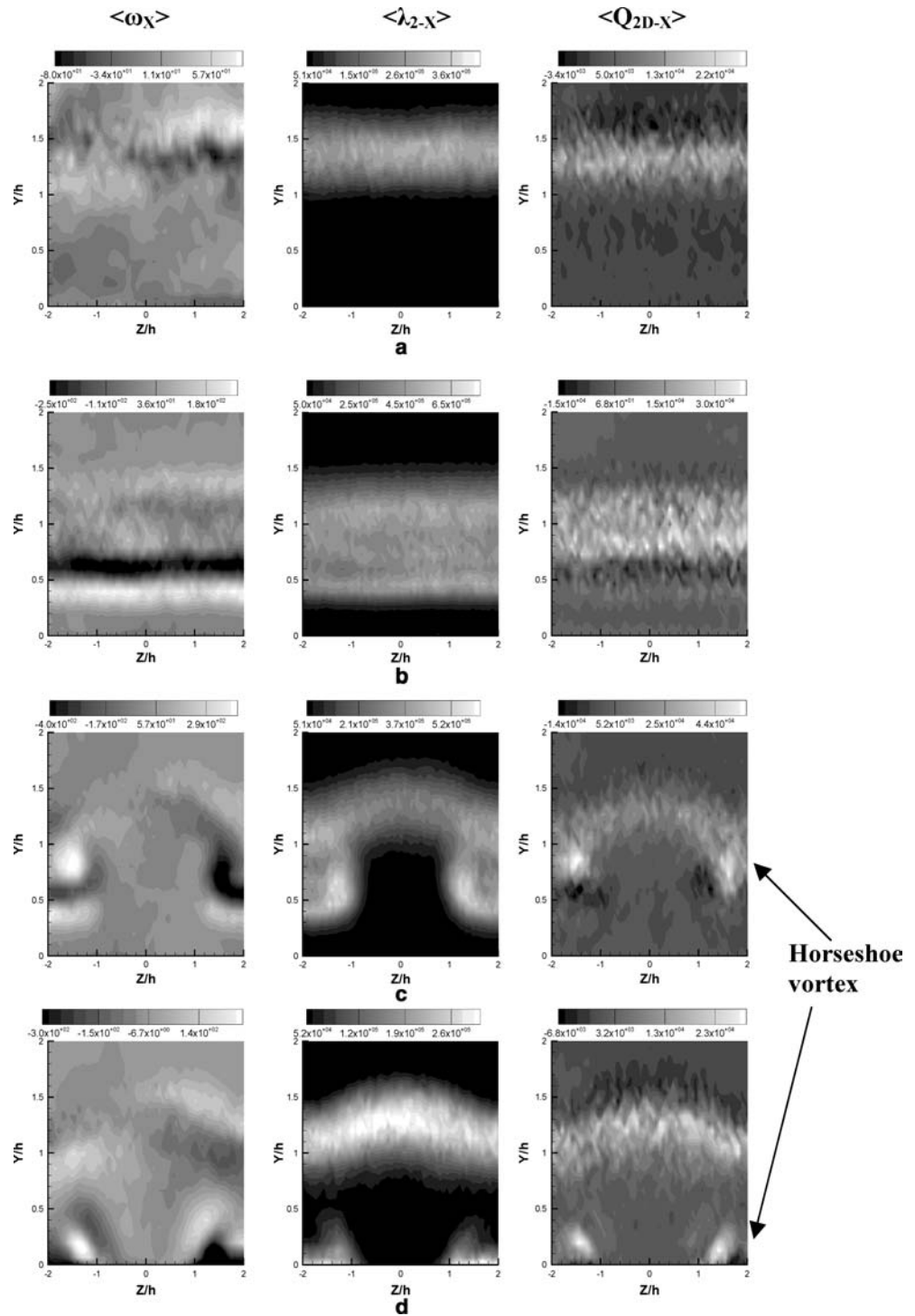
Fig. 12 The average spanwise vorticity ($\langle \omega_z \rangle$) and the coherent structure identification parameters ($\langle \lambda_{2-z} \rangle$, $\langle Q_{2D-z} \rangle$) behind different rib turbulators at $Z/h = 0$: **a** solid rib, **b** slit rib **c** split-slit rib and **d** inclined split-slit rib



cross-stream (Y) direction. Therefore, greater interaction between the vortices from the flow through the slit and the reattaching shear layer is indicated. For the split-slit rib, large value of vorticity is observed at both sides of the splitter. The high λ_{2-X} and Q_{2D-X} values at both sides of the splitter of the split-slit rib in Fig. 13c indicate the strong presence of swirling motion due to the horseshoe vortex ($Y/h \approx 0.8$). The high vorticity at $Y/h \approx 0.5$ location of the split-slit rib can be attributed to the shear in the flow through the slit. For the in-

clined split-slit rib, the large λ_{2-X} and Q_{2D-X} values successfully show the presence of horseshoe vortices near the wall ($Y/h \approx 0.2$) at both sides of the splitter (Fig. 13d). The rotational nature of streamline in the near wall region of inclined split-slit rib in Fig. 10a can be correlated to the horseshoe vortices of Fig. 13d. The bending of streamline in Fig. 10a and the clear foci in Fig. 10b at $Y/h \approx 1.2$ location correlate to the high λ_{2-X} and Q_{2D-X} values of inclined split-slit rib at similar location in Fig. 13d.

Fig. 13 The average streamwise vorticity ($\langle \omega_X \rangle$) and the corresponding average vortex structure identification parameters ($\langle \lambda_{2-X} \rangle$, $\langle Q_{2D-X} \rangle$) behind different rib turbulators at $X/h=0.5$: **a** solid rib, **b** slit rib, **c** split-slit rib and **d** inclined split-slit rib



The λ_{2-X} and Q_{2D-X} calculation clearly shows the presence of horseshoe vortices for the split-slit and inclined split-slit ribs. Praisner et al. (2001) observed horseshoe vortex in the flow around the juncture of a surface mounted cylinder based on the cross-stream vorticity field. Both the flow around the splitter and surface mounted cylinder shows identical horseshoe vortical structures due to their analogous geometry. Praisner et al. (2001) also reported a relationship

between the time mean flow structures (horseshoe vortex) and heat transfer. Therefore, the presence of horseshoe vortices behind the split-slit and inclined split-slit ribs may be responsible for higher heat transfer enhancement in these rib geometries. The appearance of streamwise vorticity due to the horseshoe vortices is expected to raise the base pressure behind the permeable ribs. Therefore, the pressure penalty is expected to be lower for the permeable ribs.

This interpretation is in agreement with 23% heat transfer enhancement and 10% reduction in pressure penalty observation of Tariq (2004) for an inclined split-slit ribbed duct compared to that of solid rib.

4.6 Fluctuation statistics

4.6.1 Streamwise plane

The non-dimensional turbulent kinetic energy $((u_{rms}^2 + v_{rms}^2)^{0.5}/U_o)$ in the streamwise direction (X - Y plane) has been compared for different rib geometries

in Fig. 14. The turbulent kinetic energy increases from the near wall region and is maximum inside the shear layer ($1 < Y/h < 2$) and subsequently drops towards the free stream. Islam et al. (2002) reported similar variation of turbulent kinetic energy in a rib roughened rectangular channel. The maximum turbulent intensity value locations in Fig. 14 do not correlate to the eye of the primary recirculation bubble location in Fig. 9. However, the maximum turbulence intensity contour of Fig. 14 shows good correlation with the spanwise vorticity distribution of Fig. 11 inside the shear layer. The high value of turbulent kinetic energy in the shear layer region is due to higher turbulence production by

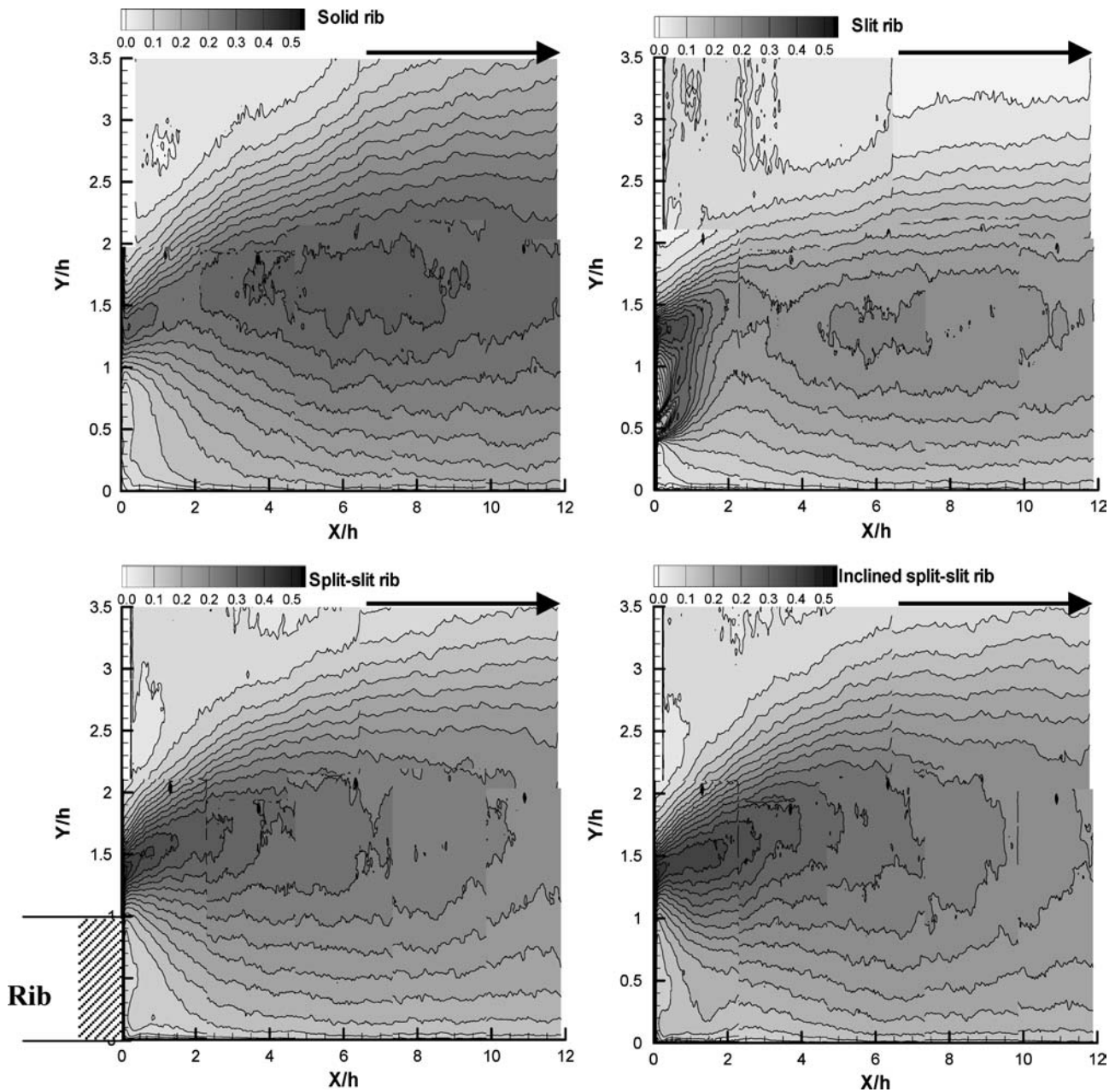


Fig. 14 The turbulence intensity $((u_{rms}^2 + v_{rms}^2)^{0.5}/U_o)$ distribution behind different rib turbulators in the streamwise (X) direction

the turbulent shear stress and velocity gradient. The trend of turbulent kinetic energy in Fig. 14 is similar to that of λ_{2-Z} and Q_{2D-Z} in Fig. 12. This indicates greater correlation between the swirling motion (high λ_{2-Z} and Q_{2D-Z} value) and the turbulent kinetic energy. This can further be verified by comparing Fig. 14 with Fig. 11, where the high near wall vorticity does not lead to high turbulent intensity at similar locations. The presence of a splitter in case of split-slit and inclined split-slit ribs leads to spanwise (Z) variation of the velocity distribution in Fig. 10. This velocity gradient in Z -direction is expected to enhance the vorticity by stretching mechanism $(\omega \cdot \nabla)V$. The locations of maximum ω_Z -vorticity in Fig. 11 correspond to that of maximum spanwise velocity gradient inside the reattaching shear layer of Fig. 10. Therefore, vorticity enhancement by vortex stretching leads to high turbulence intensity of split-slit and inclined split-slit ribs. At the downstream bottom rib corner ($Y/h \approx 0.1$), the split-slit and inclined split-slit ribs show higher turbulence compared to the solid and slit ribs possibly due to the stretching of the corner vortices (Fig. 14).

4.6.2 Cross-stream plane

The total turbulent kinetic energy $((u_{rms}^2 + v_{rms}^2 + w_{rms}^2)^{0.5} / U_o)$ in different cross-stream planes ($X/h = 0.5, 1.5, 2.5$ and 3.5) for different rib geometries have been compared in Fig. 15. The cross-stream (Y) extent with high turbulent fluctuation value increases in the streamwise (X) direction for the solid rib. The turbulent fluctuation is stronger inside the shear layer. The maximum turbulent fluctuation for the solid rib takes place at $Y/h \approx 1.4$ location for the $X/h = 0.5$ plane, which is similar to the location of vorticity maxima in Fig. 13. In the near field region ($X/h = 0.5$ and 1.5) of the solid rib, the high turbulent kinetic energy region correlates with the high velocity gradient zone (see Fig. 10) indicating the importance of the turbulent production mechanism. However, at later locations ($X/h = 2.5$ and 3.5) the turbulent kinetic energy distribution is broadened in Y -direction with weak dependence on the velocity gradient indicating the importance of other mechanism, i.e. turbulent convection and diffusion. The maximum turbulent peak intensity for the slit rib at $X/h = 0.5$ location is observed at two Y/h locations, i.e. $Y/h \approx 0.8$ and 1.2 (Fig. 15). Comparison with Fig. 10a indicates this region to be the high shear region. The maximum turbulence intensity region for the slit rib at $X/h = 0.5$ location (Fig. 15) does not take place at similar Y/h location of high vorticity magnitude in Fig. 13. The turbulent kinetic energy for the slit rib at $X/h = 0.5$ shows high value in a broad cross-stream (Y) region, i.e. between $Y/h = 0.4$ and 1.4 . However, the λ_{2-X} and Q_{2D-X} distribution in Fig. 13 is similar to the turbulent kinetic energy trend of Fig. 15 with identical cross-stream extent indicating greater correlation between turbulence and the rotational motion for the slit rib. The turbulent kinetic

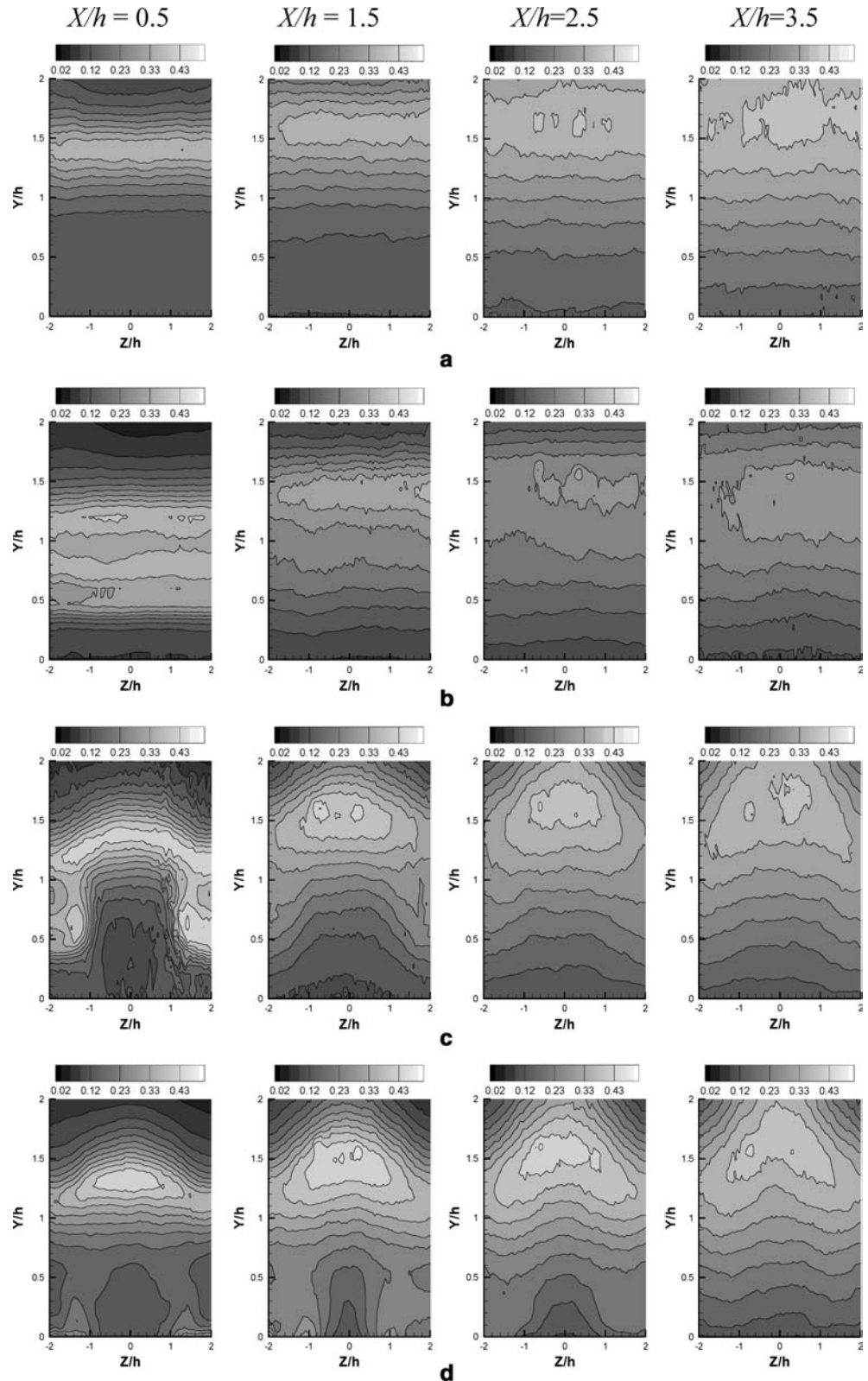
energy at later X/h locations broadens in the cross-stream (Y) direction with higher near wall turbulent fluctuation for the slit rib compared to the solid rib.

The turbulent kinetic energy magnitude of split-slit rib in Fig. 15 shows high value in the high velocity gradient region (Fig. 10). The presence of splitter leads to additional spanwise velocity gradient region (Fig. 10) leading to high turbulence intensity around it (Fig. 15). The turbulent kinetic energy at $X/h = 0.5$ location for the split-slit rib in Fig. 15 shows greater correlation with the λ_{2-X} and Q_{2D-X} distribution of Fig. 13 than the ω_X -distribution. The turbulent kinetic energy for the split-slit rib in Fig. 15 shows a high value at the horseshoe vortex location. At later X/h locations, the turbulent kinetic energy has similar distribution as the velocity gradient results of Fig. 10. The peak turbulent intensity region at later X/h locations compared to the $X/h = 0.5$ location moves upwards in Y -direction due to the upward shift of the reattaching shear layer. The peak value of turbulence intensity located at about $Y/h \approx 1.5$ location in Fig. 15 corresponds to the Y -location of high spanwise vorticity (ω_Z) in Fig. 11. This peak turbulence intensity value may be correlated to the vortex stretching mechanism. The turbulent kinetic energy in the near wall region for the split-slit rib is higher compared to that of solid and slit rib. The turbulent kinetic energy distribution of the inclined split-slit rib at $X/h = 0.5$ location in Fig. 15 shows higher value at the location of horseshoe vortices (see Fig. 13). Another zone of high turbulence intensity can be seen at about $Y/h = 1.25$ location and strong swirling motion has also been predicted from the λ_{2-X} and Q_{2D-X} results in Fig. 13. This Y/h location corresponds to the free stream focus of the vortical structure seen in Fig. 10b and c. Figure 11 shows high ω_Z -vorticity at $Y/h \approx 1.5$ location and Fig. 10 shows high spanwise velocity gradient at similar Y -location indicating greater contribution to the high turbulence intensity by vortex stretching mechanism. The maximum turbulent energy of the inclined split-slit rib shows higher value both in the nearwall and shear layer region compared to other rib geometries. It may be recalled that Tariq (2004) observed highest heat transfer enhancement for the inclined split-slit rib. The high value of turbulence intensity in the near wall region of inclined split-slit rib indicates some relationship between heat transfer enhancement and turbulence.

4.7 Flow structures

The detailed flow field measurements in both cross-stream and streamwise planes and surface flow visualization have been carried out to understand the predominant flow structures behind different rib geometries. The schematic of significant mean flow structures has been proposed in Fig. 16.

Fig. 15 The turbulence intensity $((u_{\text{rms}}^2 + v_{\text{rms}}^2 + w_{\text{rms}}^2)^{0.5} / U_0)$ at cross-stream planes ($X/h = 0.5, 1.5, 2.5, 3.5$) for different rib geometries: **a** solid rib, **b** slit rib, **c** split-slit rib and **d** inclined split-slit rib



The approaching boundary layer towards the solid rib is deflected upward over the top surface of the rib and subsequently reattaches at a downstream location. The upward deflection of the boundary layer leads to an

upstream small recirculation bubble, which meets the approaching flow at a saddle line ahead of the rib. The reattaching shear layer splits at the reattachment region and travels in opposite direction at another saddle line.

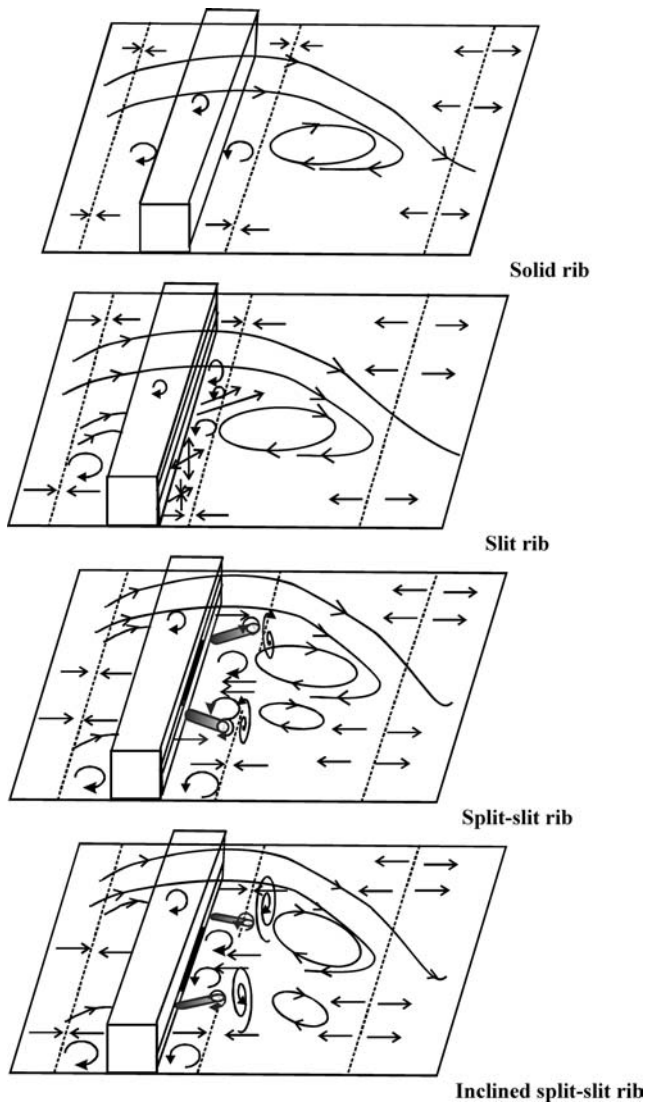


Fig. 16 The schematic of flow patterns behind different rib geometries

The primary recirculation bubble and the secondary corner vortex located behind the rib are separated from each other by a third saddle line. The reattaching shear layer near the top rib corner produces series of vortices with both ω_x and ω_z vorticity convecting in the downstream flow direction.

The flow over the slit rib shows similar critical points, i.e. upstream saddle line, two downstream saddle lines, primary recirculation bubble and secondary corner vortex as the solid rib. In addition to that, the approaching flow boundary layer for the slit rib gets disrupted upstream of the slit rib and an accelerating flow subsequently travels through the slit. This flow through the slit emerges like a jet, which travels upward and interacts with the reattaching shear layer and the primary recirculation bubble. Two additional secondary recirculation bubbles are present at the downstream top rib corner between the reattaching shear layer and the flow through the slit. The reverse flow near the bottom

test surface, the flow through the slit and the reattaching shear layer lead to line node-saddle patterns behind the slit rib.

For the split-slit rib, the approaching boundary layer moves upward over the top rib surface, which reattaches on the bottom wall and subsequently travels both upstream and downstream at the saddle location. The approaching flow through the slit bifurcates near the splitter leading to the generation of two horseshoe vortices, which come out from the slit at both sides of the splitter. Two additional corner vortices are also present near the splitter corner. The saddle line located adjacent to the downstream rib corner between the primary recirculation bubble and the secondary corner vortex is disrupted by these two corner vortices in contrast to the continuous saddle line observed for the solid and slit rib. The primary recirculation bubble size in the Y -direction reduces from behind the splitter centre ($Z/h=0$) location in the spanwise Z -direction leading to a spanwise symmetrically varying recirculation bubble. Two vortices with free slip foci are observed around the centre plane ($Z=0$) of the splitter.

The flow over the inclined split-slit rib bifurcates near the upstream rib corner: one part travels through the inclined slit and the other reattaches at the downstream line saddle. The upstream separation near the splitter face leads to the generation of two horseshoe vortices, which comes out of the slit at both sides of the splitter in the near wall region. Due to the interaction with the bottom wall, the horseshoe vortices have an irregular shape compared to that of the split-slit rib. Two corner vortices of larger size and strength compared to that of the split-slit rib are generated around the splitter. The flow through the inclined slit travels on the bottom test surface like a film flow and meets the reverse flow from the primary recirculation bubble at a saddle line. This saddle line is disrupted into two parts because of the two corner vortices. The two corner vortices drag the flow from the primary recirculation bubble around their symmetry line, which meets the downstream face of the rib. The primary recirculation bubble changes its shape and size in the Z -direction from the symmetry plane ($Z/h=0$) with two standing vortices having free slip foci around it in the near field region.

5 Conclusions

A study on flow past surface mounted permeable ribs, i.e. solid, slit, split-slit and inclined split-slit ribs has been carried out using PIV (2-C and 3-C) and surface flow visualization. The PIV measurements have been carried out in streamwise (X - Y) and cross-stream (Y - Z) planes. Both the transverse and longitudinal component of vorticity along with the mean and fluctuating velocity statistics have been reported. The 2-D eigen value and second invariant of the velocity gradient tensor have been computed for identification of coherent structures.

The following significant observations can be drawn from this study.

- (a) The permeable ribs have shorter reattachment length compared to impermeable ribs. The maximum drop in reattachment length compared to the solid rib, i.e. 41% is observed for the inclined split-slit rib. Shorter reattachment length leads to higher heat transfer enhancement of inclined split-slit ribs.
- (b) The splitter mounted inside the slit generates two longitudinal horseshoe vortices in the flow through the slit at both sides of the splitter. Two corner vortices formed behind the splitter drag the flow from the primary recirculation bubble region towards the rib leading to reduction in reattachment length.
- (c) Critical flow patterns with well defined nodes, saddles and foci observed in the cross-stream planes behind permeable ribs contributes to greater cross-stream mixing of the permeable ribs compared to the solid rib.
- (d) The generation and interaction between longitudinal and transverse vortical structures are responsible for higher mixing and heat transfer enhancement in permeable rib geometries. This also contributes to decrease in base pressure behind the permeable ribs with subsequent reduction in pressure drop penalty.
- (e) The splitter inside the slit contributes to high turbulence intensity inside the shear layer and at the downstream bottom rib corner by vortex stretching mechanism. The high heat transfer behind the inclined split-slit rib is related to the high turbulence intensity in the near wall region.
- (f) The 2-D approximation of eigen value (λ_2) criterion and second invariant of the velocity gradient tensor invariant (Q_{2D}) successfully distinguish between the swirling and shearing motion. The turbulence intensity is significant in the region with strong swirling motion.
- (g) The inclination of the slit and mounting of the splitter plate inside the slit are important design variables, which hold promise for mixing/heat transfer enhancement.

Acknowledgements The authors gratefully acknowledge the Alexander von Humboldt Foundation (<http://www.humboldt-foundation.de>) for the financial support. PKP is grateful to members of the DLR PIV group for their support.

References

- Buchlin JM (2002) Convective heat transfer in a channel with perforated ribs. *Int J Therm Sci* 41:332–340
- Calluau D, David L (2004) Stereoscopic particle velocimetry measurements of the flow around a surface-mounted block. *Exp Fluid* 36:53–61
- Dutta P, Hossain A (2005) Internal cooling augmentation in rectangular channel using two inclined baffles. *Int J Heat Fluid Flow* 26(2):223–232
- Faramarzi J, Logan E (1991) Reattachment length behind a single roughness element in turbulent pipe flow. *ASME J Fluid Eng* 113:712–714
- Gao X, Sunden B (2004) PIV measurement of the flow field in rectangular ducts with 60° parallel, crossed and V-shaped ribs. *Exp Therm Fluid Sci* 28:639–653
- Gentry MC, Jacobi AM (1997) Heat transfer enhancement by delta-wing vortex generators on a flat plate: vortex interactions with the boundary layer. *Exp Therm Fluid Sci* 14:231–242
- Heenan AF, Morrison JF (1998) Passive control of backstep flow. *Exp Therm Fluid Sci* 16:122–132
- Hwang JJ (1998) Heat transfer-friction characteristic comparison in rectangular ducts with slit and solid ribs mounted on one wall. *ASME J Heat Transf* 120:709–716
- Iacovides H, Kelemenis G, Raisee M (2003) Flow and heat transfer in straight cooling passages with inclined ribs on opposite walls: an experimental and computational study. *Exp Therm Fluid Sci* 27:283–294
- Islam MS, Haga K, Kaminaga M, Hino R, Monde M (2002) Experimental analysis of turbulent flow structure in a fully developed rib-roughened rectangular channel with PIV. *Exp Fluid* 33:296–306
- Jeong J, Hussain F (1995) On the identification of a vortex. *J Fluid Mech* 285:69–94
- Kahler CJ, Sammler B, Kompenhans J (2002) Generation and control of tracer particles for optical flow investigations in air. *Exp Fluid* 33:736–742
- Kostas J, Soria J, Chong MS (2002) Particle velocimetry measurements of a backward-facing step flow. *Exp Fluid* 33:838–853
- Liou TM, Chang Y, Hwang DW (1990) Experimental and computational study of turbulent flows in a channel with two pairs of turbulence promoters in tandem. *ASME J Fluid Eng* 112:302–310
- Liou TM, Chen SH, Shih KC (2002) Numerical simulation of turbulent flow field and heat transfer in a two-dimensional channel with periodic slit ribs. *Int J Heat Mass Transf* 45:4493–4505
- Martinuzzi R, Tropea C (1993) The flow around surface-mounted prismatic obstacles placed in a fully developed channel flow. *ASME J Fluid Eng* 115:85–92
- Panigrahi PK, Acharya S (2004) The flow over a surface mounted rib turbulator under single-mode and dual-mode excitation. *J Wind Eng Ind Aerodynam* 92:1219–1244
- Panigrahi PK, Acharya S (2005) Excited turbulent flow behind a square rib. *J Fluid Struct* 20(2):235–253
- Panigrahi PK, Tariq A (2003) Liquid crystal heat transfer measurements in a rectangular channel with solid and slit rib. *J Flow Visual* 6:407–416
- Perry AE, Chong MS (1987) A description of eddy motions and flow patterns using critical-point concepts. *Ann Rev Fluid Mech* 19:125–155
- Praisner TJ, Sabatino DR, Smith CR (2001) Simultaneously combined liquid crystal surface heat transfer and PIV flow-field measurements. *Exp Fluid* 30:1–10
- Schram C, Rambaud P, Riethmuller ML (2004) Wavelet based eddy structure education from a backward facing step flow investigated using particle image velocimetry. *Exp Fluid* 36:233–245
- Sparrow EM, Tao WQ (1983) Enhanced heat transfer in a flat rectangular duct with streamwise-periodic disturbances at one principal wall. *ASME J Heat Transf* 105:851–861
- Takase K (1996) Experimental results of heat transfer coefficients and friction factors in a 2D/3D rib-roughened annulus. *Exp Therm Fluid Sci* 13:142–151
- Tariq A (2004) Heat transfer enhancement and fluid flow transport phenomena behind surface mounted solid and permeable ribs. Dissertation, IIT Kanpur
- Tariq A, Panigrahi PK, Muralidhar K (2004) Flow and heat transfer in the wake of a surface mounted rib with a slit. *Exp Fluid* 37:701–719